SYCAMORE ALGORITHM FOR ADDRESSING CLIMATE CHANGE

[1]Hamdy Nasser, [2]Maram Essam

Abstract— The development of revolutionary technologies and the reduction of carbon dioxide in the atmosphere are the two effective strategies in dealing with current environmental issues. In the context of climate change, one goal will be to find an efficient catalyst for carbon Removal/Fixation—a process that reduces carbon dioxide by turning it into valuable chemicals. Our team has prioritized making an impact on this global issue which is developing a new quantum algorithm to simulate catalytic processes. A universal quantum computer has the potential to fundamentally change computational chemistry and areas in which strong electron correlations present severe hurdles for traditional electronic structure methods. Here, we present our analysis of accurate energy measurement and CO_2 removal efficiency on a quantum computer for computational catalysis, using improved quantum algorithms with more than an order of magnitude improvement over the best previous algorithms. As a prototypical example of local catalytic chemical reactivity, we consider the case of the Ru catalyst that can remove, capture, and transform carbon dioxide into high-value chemical methane. We created a Dual Function Material consisting of supported sodium carbonate in intimate contact with dispersed Ru as a promising catalytic solution for achieving our purposes. The Ru-Na_2CO_3 material deposited in the area of our physical demonstration (Air), captures CO_2, and catalytically converts it to synthetic natural gas (methane) using H_2 existing in the atmosphere. This material functions well in O_2 (Air) and H_2O (Ocean) containing massive amounts of CO_2. We aim at accurate resource estimates for enhancing the mechanism of our reaction and the removal efficiency of the catalyst through the great insight from assessing the electronic energy of key intermediates and transition states of its catalytic cycle. In particular, we present new quantum algorithms for double-factorized representations that can significantly reduce the computational cost over previous algorithms. We address the requirements for future quantum hardware to make a universal quantum computer a successful and reliable tool for quantum computing enhanced computational chemistry. As a combined CO_2 Removal/fixation process and quantum computing technology, this technology overcomes many of the limitations of CO_2 removal catalysts which demonstrates net negative and durable CO_2 removal at Mt/y scale, is prepared to reach the Gt/y scale, and introduces a very promising solution for climate change that needs time and support to make our world carbon negative.

Keywords— Carbon Removal/Fixation – SYCAMORE Quantum System – Varitonal Quantum Eigensolver (VQE) – Unitary Coupled-Cluster (UCC) – Sabatier Reaction – Ruthinum Catalytic Reaction – Synthetic Natural Gas (SNG)

1 INTRODUCTION

As predicted by the Intergovernmental Panel on Climate Change (IPCC), carbon dioxide in the atmosphere may reach 570 ppmv by the year 2100, accompanied by a rise in the mean global temperature of 1.9 ◦C and mean sea level by 38 cm. Excess carbon dioxide emission results primarily from anthropogenic activities by fossil fuel combustion for power generation, industrial manufacturing, and transportation. Due to the CO2 accumulation and the rising demand for energy, CO2 capture, and sequestration are the most efficient method to combat greenhouse gas emissions and associated climate change.

For a decade, various processes and materials have been proposed for CO2 capture, with extensive reviews available. Carbon Removal/Fixation technology is still the most popular and developed approach toward capturing CO2 from the air. Our goal is to find an efficient catalyst for the carbon removal/fixation process. Currently, synthetic catalytic processes are found through lengthy trial-and-error lab experiments. In a process that requires testing thousands of molecular combinations, computer simulations that very accurately model quantum correlations could replace the complex synthesis of new candidate catalysts. Whereas computers today can have a difficult time accurately calculating properties of complex molecules, quantum computers are especially suited for this task and will give more reliable and predictive simulation results. Quantum computing has the potential to efficiently solve some computational problems that are exponentially hard to solve on classical computers. Among these problems, one of the most prominent cases is the calculation of quantum electronic energies in molecular systems that can reveal the secrets of a specific reaction or lead to new discoveries about it. Due to its many applications in chemistry and materials science, this problem is widely regarded as the "killer application" of future quantum computers.

A prerequisite for this ability to predict chemical processes is an understanding of the underlying reaction mechanisms. Quantum mechanics allows one to assign energies to molecular structures so that a comparison of these energies in a sequence of molecular transformations can be taken as a measure to rate the viability of such a chemical reaction. Relative energies are a direct means to predict reaction heats and activation barriers for chemical processes. However, the

- *Hamdy Nasser is a young researcher in Quantum Computation in Egyptian Space Agency, Egypt. E-mail: hamdy.1019112@stemoctober.moe.edu.eg*
- *Maram Essam is a young researcher in Chemistry in Egyrtian Space Agency, Egypt. E-mail: maram.2119147@stemkalubya.moe.edu.eg*

reliability of such predictions depends crucially on the accuracy of the underlying energies, of which electronic energy is often the most important ingredient. This energetic contribution of the dynamics of the electrons in a molecule can be calculated by solving the electronic Schrodinger equation, typically done on a so-called one-particle basis, the set of molecular orbitals.

The computational complexity of an exact solution of the electronic Schrodinger equation on classical computers is prohibitive as the many-electron basis expansion of the quantum state of interest grows exponentially with the number of molecular orbitals (often called the "curse of dimensionality"). The exact diagonalization of the electronic Hamiltonian in the full many-electron representation is therefore hard and limited to small molecules that can be described by comparatively few (on the order of twenty) orbitals. Once accomplished, it is said that a full configuration interaction (full-CI) solution in this finite orbital basis has been found. Since typical molecular systems will require on the order of 1000 molecular orbitals for their reliable description, exact-diagonalization methods need to restrict the orbital space to about twenty orbitals chosen from the valence orbital space (called complete active space (CAS) CI). Accordingly, approximate methods have been developed in quantum chemistry for large orbital spaces. By contrast, quantum computing allows for encoding of a quantum state in many qubits that scale linearly with the number of molecular orbitals and have therefore the potential to deliver full-CI solutions for large orbital spaces that are inaccessible to traditional computing because of the exponential scaling.

In this work, we, therefore, revisit the problem of quantum computing enhanced reaction mechanism elucidation with a focus on a specific chemical reaction that is prototypical for carbon removal catalysis. The example that we chose is the catalytic removal/fixation of carbon dioxide, i.e., the capture of the greenhouse gas carbon dioxide by a catalyst that removes, activates, and eventually transforms it into a useful chemical. Furthermore, we extend our work concerning the steps that need to be carried out by a quantum computer, specifically regarding the resources of the state preparation step. In our work, there has been significant progress in quantum algorithms, but also a better understanding of what it takes to build a scalable quantum computer has been reached. On the algorithmic side, Hamiltonians represented by a linear combination of unitaries in a so-called Blackbox query model can now be simulated with optimal cost using techniques called "qubitization" and "quantum signal processing". In addition, structure in broad families of Hamiltonians can be exploited to reduce the cost of the simulation even more. This includes Hamiltonians with geometrically local interactions and large separations in energy scales. Even more recently, very promising tight theoretical bounds on the performance of traditional Lie-Trotter-Suzuki formulas on average-case Hamiltonians have been obtained. We have considered realistic assumptions for mid-term quantum hardware.

Therefore, we also discuss the overhead due to mapping the quantum algorithm to a two-dimensional planar layout, which further increases the overall runtime but makes the estimates more realistic. After we have conducted our calculations of the electronic energies and the transition states of our specified chemical reaction, we have discussed the enhanced issues we added to the reaction that boosted the efficiency and the progression of the molecules during the reaction.

A HOMOGENEOUS CARBON DIOXIDE FIXATION CATALYST

The infrared absorption properties of carbon dioxide make it a greenhouse gas that is a major contributor to climate change. Naturally, limiting or even inverting rising carbon dioxide levels in the atmosphere is a truly important goal, and all possible ways to accomplish it must be considered. In basic research, options have been explored to remove and fix carbon dioxide to yield chemicals of higher value. Not many catalysts have been reported so far that can transform carbon dioxide directly into methane and all of these are plagued by a comparatively low turnover number. To find synthetic catalysts that robustly produce high-value chemicals from carbon dioxide with a high turnover number is, therefore, an important design challenge and computational catalysis can provide decisive insights as well as virtual screening to meet this challenge. The process of catalyst selection is based on the ability of carbon adsorption and fixation. One of the most promising catalysts, we have found, is the Ruthenium catalyst (Ru).

The presentation of the CO2-fixating ruthenium catalyst was accompanied by extensive DFT calculations of the potentially relevant molecular structures, which is a routine procedure in chemistry. However, DFT electronic energies are plagued by approximations made to the exchange-correlation functional. The authors of Ref. [1] selected the Minnesota functional M06-L because they found good overall agreement with their experimental results. In order to demonstrate the uncertainty that generally can affect DFT results, which can be very cumbersome if experimental data are not available for

comparison, we supplemented the DFT data of Ref. [1] with results obtained with the standard generalized-gradient-approximation functional PBE and its hybrid variant PBE0 for the eight structures, (shown in Fig. 1), of the reaction mechanism considered in this work (data shown in Fig. 2). As can be seen in Fig. 2, whereas structure optimization has a small effect on the relative electronic energies, the difference between the functionals can amount to more than 50 kJ/mol (i.e., 19 mHartree per molecule) and can even reverse the qualitative ordering of the compounds (compare structures 'V' und 'VIII'). Obviously, in the absence of any additional information (such as experimental data or more accurate calculations), it is virtually impossible to settle on reliable energetics with potentially dramatic consequences for the elucidation of a reaction mechanism.

QUANTUM COMPUTING ENHANCED COMPUTATIONAL CATALYSIS

The elucidation of chemical reaction mechanisms is routinely accomplished with approximate quantum

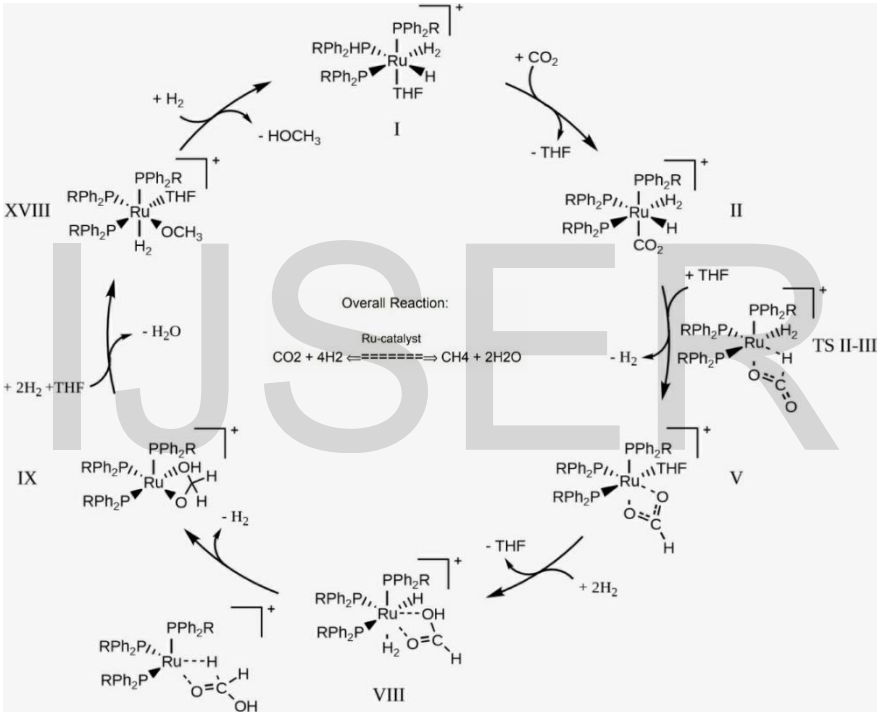

Figure 1. Selected steps of the catalytic cycle elucidated in Ref. [1] on the basis of DFT calculations: intermediates and transition state structures considered for the present work are shown (Roman numerals are according to the original publication).

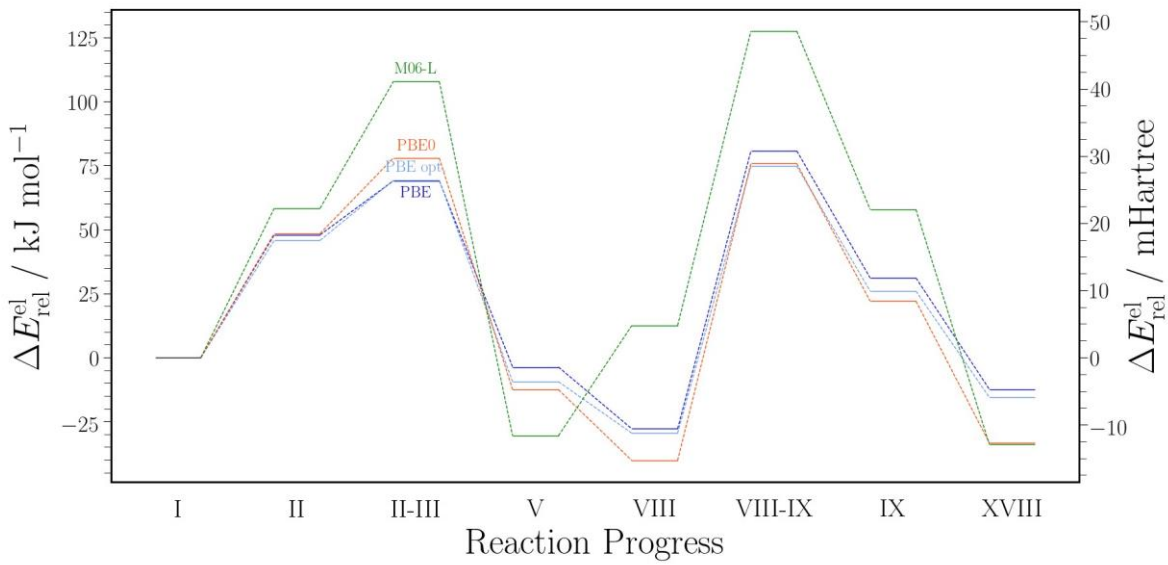

Figure 2. Relative DFT electronic reaction energies for the catalytic cycle obtained with a def2-TZVP basis set and three different approximate density functionals: M06-L [1], PBE, and PBE0 on M06-L/def2-SVP-optimized structures taken from Ref. [1]. For comparison, we provide relative electronic reaction energies from PBE/def2TZVP//PBE/def2-TZVP calculations (in Pople's double slash notation, where the density functional behind the double slash is the one for which the structure was obtained) labeled as "PBE opt.".

chemical methods, for which usually stationary structures are optimized, yielding stable reactants, products, and intermediates of a chemical process, which are key for detailed kinetic studies and hence for the prediction of concentration fluxes.

In the following, we discuss wherein the mechanism elucidation process of quantum computing can be efficient, useful, and decisive, and hence, how quantum computing can efficiently enhance and reinforce computational catalysis to make a difference. As there are many steps involved that require a deep understanding of various branches of theoretical chemistry, we provide an overview of the essential steps in Fig. 3. Understanding chemical catalysis, and chemical reactions in general, requires an exploration of relevant molecular structures (structure exploration in Fig. 3), which is usually done manually and with DFT approaches (as in Ref. [1] for our example here), but which can now also be done in a fully automated and even autonomous way. These structures need to be assigned energy which may be conveniently separated into an electronic contribution (steps 1-7 in Fig. 3) and a remaining part (additional free energy calculations in Fig. 3). Relative free-energy differences will eventually be used as barrier heights in expressions for absolute rate constants (kinetic modeling in Fig. 3) that can then be used in kinetic modeling for predicting concentration fluxes through the chemical web of relevant molecular structures. Ultimately, such knowledge can be exploited to improve on existing or to design new catalysts with enhanced catalytic properties.

Accuracy matters: A reaction rate depends exponentially on the energy difference between a transition state structure and its corresponding stable reactants, which are connected by an elementary reaction step. Because of this exponential dependence, highly accurate energy differences are decisive. While many contributions enter these free energy differences, the electronic energy difference is the most crucial one in bond breaking and bond-making processes.

Electronic energies are key components (steps 1-7 in Fig. 3): Electronic energies are notoriously difficult to calculate, and standard approximations are affected by unknown errors that can be large. Only for electronically simple struc-

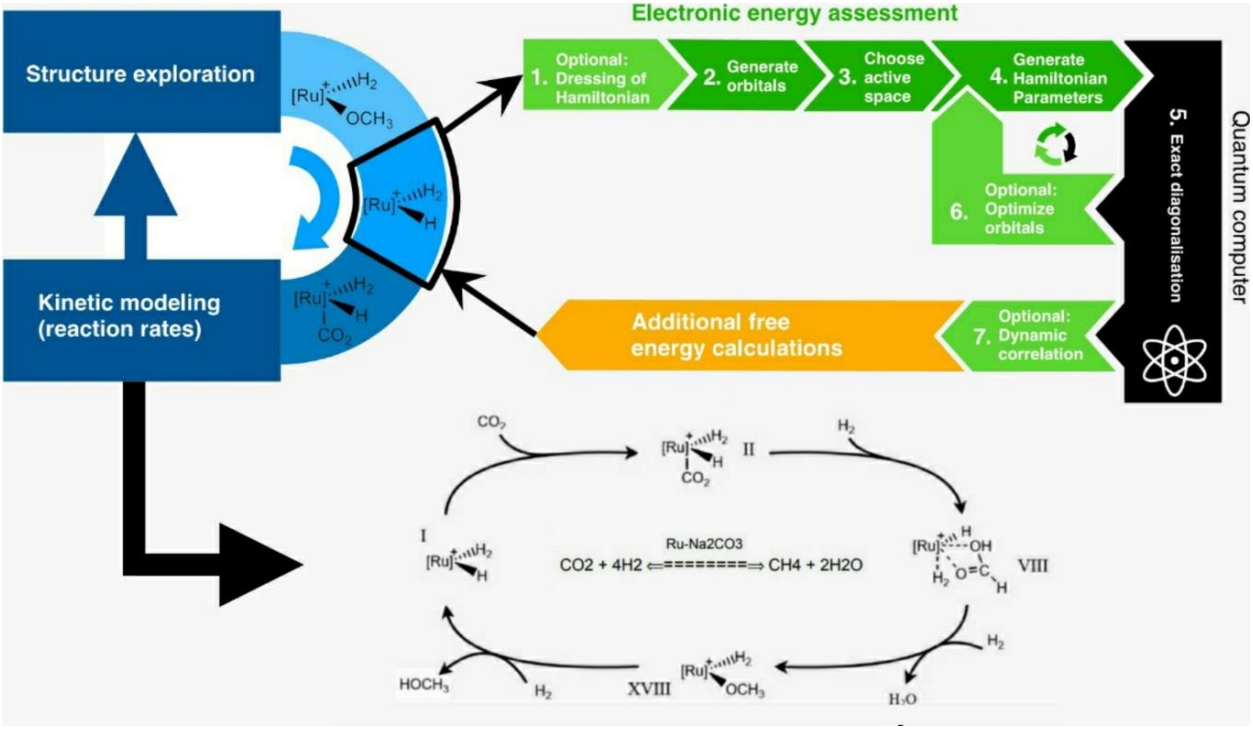

Figure 3. Protocol of computational catalysis with the key step of quantum computing embedded in black, which is usually accomplished with traditional methods such as CASSCF, DMRG, or FCIQMC (see text for further explanation)

tures, so-called closed-shell single-determinant

electronic structures, well-established methods exist that run efficiently on a classical computer (such as explicitly correlated local coupled-cluster schemes with, at least, perturbatively treated triple excitations). For general electronic structures, however, no method of comparable accuracy exists that is at the same time feasible for moderately sized molecules. In particular, for strong correlation cases, which require more than one Slater determinant for a qualitatively correct description of the electronic wave function, it can be hard to obtain an accurate total electronic energy, which then enters the calculation of relative energies. For decades, it has been the goal of quantum chemistry to devise methods that efficiently construct approximations to a many-electron state represented in terms orbitals. In our work, the full many-electron Hamiltonian constructed from such a many-electron basis is expressed and diagonalized in a complete many-electron (determinantal) basis which means that a full-CI calculation is nearly carried out. This exact diagonalization process has taken about 28 orbitals to be feasible (record calculation).

Required accuracy: A reasonable target accuracy for relative energies (and therefore also for total electronic energies of molecular species) is

about 1 mHartree, if not 0.1 mHartree. This corresponds to about 2.6 and 0.26 kJ/mol, respectively. Note that thermal energy RT (T being temperature and R the gas constant) at room temperature is on the order of 2.6 kJ/mol, which may be related to the kinetic energy of a reactant molecule at average velocity. It is important to understand that this target accuracy is important for relative energies, i.e., for the energy differences that eventually enter the rate constant expressions. For total electronic energies, however, this accuracy does not match the precision with which these energies are known. Hence, such calculations rely on significant error cancellation effects that occur when atomic contributions to the total electronic energy drop out in the calculation of reaction energies (which are relative energies) as they are conserved during a reaction (consider, e.g., a molecular orbital that is mostly of 1s-atomic orbital character and remains unaffected by a chemical reaction but contributes significantly to the total electronic energy).

Challenges of electronic structure (steps 1-7 in Fig. 3): It is, therefore, most important to get the electronic (valence) structure of each relevant molecular structure right. Here, quantum computing offers an opportunity. It is important to realize that a typical chemical catalysis problem does not involve very many valence orbitals in every elementary reaction step. As a consequence, the size of the active orbital space, from which the electronic wave function is constructed, does usually not need to be very large and can be easily handled with methods such as Complete Active Space Self Consistent Field (CASSCF), DMRG, or FCIQMC. The latter two are capable of handling active orbital spaces of up to about 100 spatial orbitals owing to efficient approximations. However, sometimes there may be a price to pay for these approximations and that is a residual uncertainty regarding the convergence of the electronic energy. For instance, a DMRG result will critically depend on – apart from a fixed finite value of the bond dimension – proper convergence of the sweeping algorithm, which, at times, might be difficult to determine. In the case of the more recent FCIQMC approach, which is under continuous development and offers extraordinarily efficient scaling on large traditional parallel computers, convergence concerning the number of walkers or extrapolation to an infinite number of walkers may be hard to achieve for certain molecules. We also note that it is generally hard for any quantum chemical approach (hence, also for DMRG and FCIQMC) to deliver rigorous yet useful information about the error associated with a specific result. In our upcoming work, we will solve the challenge of electronic structure and the convergence of electronic energy.

Quantum computing is supposed to be a valuable and, in the long run, ultimately superior competitor to the aforementioned traditional methods (i) because rigorous error estimates are available and (ii) because systems are accessible that are traditionally not feasible because of the curse of dimensionality when a total state is to be represented in a large set of orbitals. Consequently, we have obtained novel and hardly reachable results that came with great benefits and crucial discoveries about our catalytic reaction to being considered as a killer application in the area of carbon dioxide removal catalysts.

QUANTUM ALGORITHMS FOR CHEMISTRY

For the catalysis problem, we require quantum algorithms that provide reliable results with controlled errors on the electronic energy on a given orbital basis. Uncontrolled approximations in quantum algorithms would negate the advantages offered by quantum computers, which will require tremendous effort to build and operate even at a moderately sized error-corrected scale. Though it is without a doubt that the popular variational quantum eigensolver (VQE) can obtain parameters of a unitary coupled-cluster (UCC) parametrization of the electronic wavefunction that is likely to be accurate (especially when higher than double excitations are considered), unlike all the best used structures, this scheme is specialized with degenerating residual unknown uncertainties in the true electronic energy. Thus, reducing the errors of our calculation by improving the ansatz (wave function) will require significantly less gate operations than are expected. Moreover, our system made the number of repetitions required to estimate energies with sufficient accuracy of 1 mHartree or better small. We also note that knowledge of reliable and controllable errors in quantum algorithms is a decisive advantage over classical methods such as DMRG and FCIQMC as convergence control for their parameters is not necessarily easy or even feasible.

Therefore, we turn to one of the most promising applications of quantum computers, which is a bounded-error simulation of quantum systems using quantum phase estimation. The main idea is to synthesize a quantum circuit that implements the real time-evolution operator $W = e^{-iH/a}$ by a given Hamiltonian H for some normalizing factor a, which henceforth are always in atomic units of Hartree.

$$_1 - \ _2|$$
$$\times \psi_k^*(x_2)\psi_l(x_2)\mathrm{d}^3x_1\mathrm{d}^3x_2, \qquad (4)$$

When applied n times to an eigenstate $H|\psi\rangle = E_k|\psi_k\rangle$, a phase nE_k/a is accumulated. Quantum phase estimation then estimates the energy E_k with a standard deviation $\Delta_E = \mathrm{O}(a/n)$.

If one prepares an arbitrary trial state $|\psi_{\mathrm{trial}}\rangle$ rather than an eigenstate, phase estimation collapses the

trial state to the k-th eigenstate with probability $p_k = |\langle h\psi_k | \psi_{\text{trial}} \rangle|^2$ and it returns an estimate to the corresponding energy E_k.

The phase estimation procedure is executed on a quantum computer by applying a sequence of quantum gates. If the unitary W is implemented using a number c_W of quantum gates, the overall quantum gate cost of obtaining a single estimate $\hat{E}_k$ is then

$$c_W \times \frac{\pi\alpha}{2\Delta_E}, \quad (1)$$

where the factor $\frac{\pi\alpha}{2\Delta_E}$ arises from previous analyses on the performance of phase estimation (combined with a so-called phase-doubling trick). In general, the quantum circuit only approximates W to some bounded error Δ_W in spectral norm. This adds a systematic bias of $a\Delta_W$ to the estimate $\hat{E}_k$. Thus, we budget for this error by making the somewhat arbitrary choice of performing phase estimation to an error of $0.9\Delta_E$, and compiling W so that $\Delta_W \leq 0.1\Delta_E/a$. To date, there are several prominent quantum algorithms for approximating real time-evolution, such as Lie-Trotter-Suzuki product formulas, sparse Hamiltonian simulation, linear-combination of unitaries, qubitization, and quantum signal processing. In this work, we consider the electronic Hamiltonian in its non-relativistic form with Coulomb interactions (in Hartree atomic units),

$$H = \sum_{ij,\sigma} h_{ij} a^\dagger_{(i,\sigma)} a_{(j,\sigma)} + \frac{1}{2} \sum_{ijkl,\sigma\rho} h_{ijkl} a^\dagger_{(i,\sigma)} a^\dagger_{(k,\rho)} a_{(l,\rho)} a_{(j,\sigma)} \quad (2)$$

which is parametrized through the one- and two electron integrals h_{ij} and h_{ijkl} of the molecular orbitals $\{\psi_i\}$,

$$T = \begin{bmatrix} 1 & 0 \\ 0 & \sqrt{i} \end{bmatrix} \qquad h_{ij} = \int \psi_i^*(x_1) \left(-\frac{\nabla^2}{2} - \sum_m \frac{Z_m}{|x_1 - r_m|} \right) \times \psi_j(x_1) \mathrm{d}^3 x_1, \quad (3)$$

$$h_{ijlk} = \int \psi_i^*(x_1) \psi_j(x_1) \left(\frac{1}{|x \quad x} \right)$$

where x_i denote electronic coordinates and Z_m is the charge number of nucleus m at position r_m (note that a relativistic generalization is straightforward). We explicitly separate the fermion indices $p \equiv (i,\sigma)$ into an index where $i \in \{1,\ldots,N\}$ enumerates the N spatial molecular orbitals, and $\sigma \in \{0,1\}$ indexes spin-up and spin down. Hence, the fermion operators satisfy the usual anti-commutation relations

$$\{a_p, a_q\} = 0, \quad \{a_p^\dagger, a_q^\dagger\} = 0, \quad \{a_p, a_q^\dagger\} = \delta_{pq}\mathcal{I}, \quad (5)$$

and the coefficients h_{ij}, h_{ijkl} are real and satisfy the symmetries

$$h_{ij} = h_{ji}, \quad (6)$$

$$h_{ijkl} = h_{jikl} = h_{ijlk} = h_{jilk} = h_{lkij} = h_{lkji} = h_{klij} = h_{klji}.$$

For the purposes of phase estimation through the so-called *qubitization* approach, it is not necessary to simulate time-evolution e^{-iHt}, but it can be advantageous in some cases to implement the unitary walk operator $W = e^{i\sin^{-1}(H/a)}$ instead, which has some normalizing constant $a \geq H$ that ensures the arcsine is real. This walk operator can be implemented exactly, assuming access to arbitrary single-qubit rotations, in contrast to all known quantum algorithms where time-evolution e^{-iHt} can only be approximated. After estimating the phase $\hat{\theta} = \sin^{-1}(E_k/a)$ with phase estimation, we may obtain $\hat{E}_k$ by applying $\sin(\hat{\theta})$ in a classical postprocessing step.

We focus on the qubitization technique applied to electronic structure Eq. (2), with the goal of minimizing the quantum gate costs in Eq. (1). In fault-tolerant architectures, quantum gate costs reduce to the number of so-called primitive Clifford gates (e.g. Hadamard= $\frac{1}{\sqrt{2}}\begin{bmatrix} 1 & 1 \\ 1 & -1 \end{bmatrix}$, phase= $\begin{bmatrix} 1 & 0 \\ 0 & i \end{bmatrix}$, and controlled-Not) and non-Clifford gates (e.g. and Toffoli, which applies a Not gate controlled on two input bits being in the 'one' state). As the physical resources needed to implement a single error-corrected primitive non-Clifford gate, such as the T gate is on the order of 100 to 10000 times more costly than a single two-qubit Clifford gate – and one Toffoli gate may be implemented by four T gates – much recent work has focused on optimizing the non-Clifford gate cost of W. Within an atom-centered basis set (such as the ones employed in this

work), this focus has reduced the T gate cost of obtaining a single estimate $E\hat{}_k$ from $O\tilde{}(N^5/\Delta^{3/2}{}_E)$ using Trotter methods to $O\tilde{}(a_{CD}N^{3/2}/\Delta_E)$ Toffoli gates and $O(N^{3/2}\log N/\Delta_E)$ qubits using qubitization combined with a so-called single-factorized Hamiltonian representation, where $a_{CD} = O(N^3)$ is a certain norm of the Hamiltonian. Our main technical contribution is a further reduction of the gate cost of W and the normalizing factor to $a_{DF} = O(N^{3/2})$ as described in the next Section.

EFFICIENT ENCODING OF DOUBLE-FACTORIZED ELECTRONIC STRUCTURE

Our main algorithmic advance is based on a quantum algorithm to 'qubitize' the so-called double factorized representation H_{DF} of the electronic Hamiltonian H. On the one hand, the double factorized representation is sparse, and therefore minimizes the cost c_W of qubitization, which generally scales with the number of terms needed to represent the Hamiltonian. On the other hand, the double-factorized representation is a partial diagonalization of the original Hamiltonian, and hence has a small normalizing constant a_{DF}. Despite these favorable properties, previous quantum simulations using this representation are based on Trotter methods.

The double-factorized form builds upon the single factorized representation H_{CD} of the Hamiltonian H were,

$$H_{CD} \doteq \sum_{ij,\sigma} \tilde{h}_{ij} a^\dagger_{(i,\sigma)} a_{(j,\sigma)} + \frac{1}{2} \sum_{r\in[R]} \left(\sum_{ij,\sigma} L^{(r)}_{ij} a^\dagger_{(i,\sigma)} a_{(j,\sigma)} \right)^2 \quad (7)$$

$$\tilde{h}_{ij} \doteq h_{ij} - \frac{1}{2} \sum_l h_{illj}. \quad (8)$$

Note that the rank-R factorization of the two-electron tensor $h_{ijkl} = \sum_{r\in[R]} L^{(r)}_{ij} L^{(r)\top}_{kl}$ Eq. (2) into the $N \times N$ symmetric matrices $L^{(r)}$ always exists due the symmetry constraints Eq. (6) and may be computed using either a singular-value decomposition or a Cholesky decomposition. This representation also facilitates a low-rank approximation by truncating the rank R. In the worst case, $R \leq N^2$. However, it was noted. that rank $R \sim N \log(N)$ for typical molecular systems when N is proportional to the number of atoms, which is a provable statement for 1D systems. This reduces the number of terms needed to describe the second-quantized Hamiltonian from $O(N^4)$ in Eq. (2) to $O(RN^2)$ in Eq. (7). This representation was first exploited to qubitize H_{CD} with a normalizing constant $a_{CD} \triangleq 2 \| \tilde{h} \|_{EW} + 2 \sum_{r\in[R]} \| L^{(r)} \|^2_{EW}$ expressed using the entry wise norm.

The technical innovation in our approach is a quantum circuit, detailed in the supplementary material, for qubitzing the double-factorized Hamiltonian

$$H_{DF} = \sum_{ij,\sigma} \tilde{h}_{ij} a^\dagger_{(i,\sigma)} a_{(j,\sigma)} + \frac{1}{2} \sum_{r\in[R]} \left(\sum_{ij,\sigma} \sum_{m\in[M^{(r)}]} \lambda^{(r)}_m \vec{R}^{(r)}_{m,i} \vec{R}^{(r)}_{m,j} a^\dagger_{(i,\sigma)} a_{(j,\sigma)} \right)^2 . \quad (9)$$

This is obtained by a rank $M^{(r)}$ eigen decomposition of the symmetric matrices $L^{(r)} = \sum_{m\in[M^{(r)}]} \lambda^{(r)}_m \vec{R}^{(r)}_m \cdot (\vec{R}^{(r)}_m)^\top$ $(R^{(r)}_m)^T$ into a total of $M = \sum_{r\in[R]} M^{(r)}$ each normalized to be of unit length $\| R^{(r)}_m \|_2 = 1$. The number of terms in Eq. (9) is even further reduced to $O(MN)$, also noted that for typical molecular systems where $N \gg 10^3$ scales with the number of atoms, one may retain $M \sim N \log N$ eigenvectors and truncate the rest. A key technical step in our approach is to work in the Majorana representation of fermion operators

$$\gamma_{p,0} = a_p + a\dagger p, \quad (10)$$

$$\gamma_{p,1} = -i \left(a_p - a^\dagger_p \right) \quad (11)$$

$$\{\gamma_{p,x}, \gamma_{q,y}\} = 2\delta_{pq}\delta_{xy}\mathrm{I}. \quad (12)$$

As we show in the supplementary material, this representation maps

$$H_{DF} \to \left(\sum_i h_{ii} - \frac{1}{2} \sum_{il} h_{illi} + \frac{1}{2} \sum_{il} h_{llii} \right) \mathcal{I} + \mathrm{One}_{L^{(-1)}} + \frac{1}{2} \sum_{r\in[R]} \mathrm{One}^2_{L^{(r)}}, \quad (13)$$

which is expressed as a sum of squares of one-body Hamiltonians

$$L \doteq \frac{i}{2} \sum \sum_\sigma L_{ij} \gamma_{i,\sigma,0} \gamma_{j,\sigma,1}$$

$$\|L^{(r)}\|_{EW} \doteq \sum_{ij\in[N]} |L^{(r)}_{ij}|$$

$$L_{ij}^{(-1)} \doteq h_{ij} - \frac{1}{2}\sum_l h_{illj} + \sum_l h_{llij}. \quad (15)$$

(14)

This leads to a normalizing constant

$$\alpha_{\mathrm{DF}} = \|L^{(-1)}\|_{\mathrm{SC}} + \frac{1}{4}\sum_{r\in[R]} \|L^{(r)}\|_{\mathrm{SC}}^2 \quad (16)$$

Note that the difference between $L^{(-1)}$ and $\tilde{h}$ is the mean-field Coulomb repulsion contribution term $\sum_l h_{llij}$. Note that α_{DF} is also significantly smaller than α_{CD} from previous approaches []. In addition to the factor of eight reduction in the prefactor of the two-electron norms, the dependence of α_{DF} on Schatten norms $\| L^{(r)} \|_{sc}$ is beneficial as they can be up to a factor of N smaller than the entry-wise norms $\| L^{(r)} \|_{EW}$ that α_{CD} depends on, as follows from the following tight inequalities for any Hermitian $N \times N$ matrix h,

$$\| h \|_{sc} = \sum \quad X\,|\mathrm{Eigenvalues}[h]k|=, \quad (17)$$

$$\frac{1}{N}\|h\|_{\mathrm{EW}} \leq \|h\|_{\mathrm{SC}} \leq \|h\|_{\mathrm{EW}} \quad (18)$$

which we prove in the supplementary material and may be of independent interest.

The Toffoli gate complexity of synthesizing the walk operator to an error $\Delta_W = 0.1\Delta_E/\alpha_{\mathrm{DF}}$, as detailed in the supplementary material, is then

$$c_W \leq \frac{2M}{1+\lambda} + 2\lambda N\beta + 8N\beta + 4N + \mathcal{O}(\sqrt{R\log M} + \sqrt{M\log(1/\Delta_W)}), \quad (19)$$

for any choice of integer $\lambda \geq 0$, and where the parameter. This $\beta = \left\lceil 5.652 + \log_2\left(\frac{N}{\Delta_W}\right)\right\rceil$ also uses the following number of qubits

$$N\beta(1+\lambda) + 2N + \mathrm{O}(\log(N/\Delta_W)). \quad (20)$$

Note that λ controls the number of ancillary qubits. By choosing, $\lambda = \mathcal{O}(\sqrt{\frac{M}{N\beta}})$ the Toffoli cost is $c_W = \mathrm{O}(\sqrt{MN\beta}+N\beta)$, which is advantageous when $M \gg N\beta$, using $\mathcal{O}(\sqrt{MN\beta}+N+\beta)$ qubits, Assuming the empirical scaling of M and R by Peng et al., our algorithm encodes electronic spectra for atom centered basis sets into the walk operator using only $c_W = \tilde{\mathrm{O}}(N)$ Toffoli gates, and with a normalizing constant α_{DF}, which improves upon the $\tilde{\mathrm{O}}(N^{3/2})$ Toffoli gates and larger normalizing constant α_{CD} required by the single-factorized approach. In the following examples we consider, typical values of λ that minimize the Toffoli costs are between 1 and 5, and the Toffoli gate counts, and qubit counts we quote exclude the subdominant big-O($\cdot$) component of Eqs. (19) and (20).

Truncation

We now describe our procedure for obtaining, by truncating eigenvalues, low-rank approximations $\tilde{H}_{\mathrm{DF}}$ of the double-factorized Hamiltonian Eq. (13) from an initial numerically exact representation H_{DF}. We focus on truncating the two-electron terms as those tend to dominate the cost of block-encoding. Given a target approximation error , we consider two truncations' schemes, which we call *coherent* and *incoherent*. The coherent scheme upper bounds the actual error

$$\|\tilde{H}_{\mathrm{DF}} - H_{\mathrm{DF}}\| \leq \epsilon_{\mathrm{co}}, \quad (21)$$

in spectral norm for any given choice of ϵ_{co} This upper bound is obtained by a triangle inequality, which assumes that all truncated terms have an error that adds linearly. That is, if the difference $\tilde{H}_{\mathrm{DF}} - H_{\mathrm{DF}} = \sum_i h_i$ is a sum of terms, then we truncate so that

$$\sum_j \|H_j\| \leq \epsilon_{\mathrm{co}} \quad . \quad (22)$$

We find that this bound is often quite loose, and the gap between the actual error and grows with system size. This motivates the *incoherent* scheme, which assumes that the error of truncated terms adds incoherently by a sum-of-squares. Thus, we truncate so that

$$\sqrt{\sum_j \|H_j\|^2} \leq \epsilon_{\mathrm{in}} \quad . \quad (23)$$

Suppose we remove a single eigenvalue $\lambda_m^{(r)}$ from Eq. (13) during truncation. Using the identity $A^2 - (A - B)^2 = AB + BA - B^2$, the difference

$$H_{\mathrm{DF}} - \tilde{H}_{\mathrm{DF}} = \frac{1}{2}\left(\left\{\mathrm{One}_{L^{(r)}}, \frac{\lambda_m^{(r)}}{2}\sum_\sigma \gamma_{\vec{R}_m^{(r)},\sigma,0}\gamma_{\vec{R}_m^{(r)},\sigma,1}\right\} - \left(\frac{\lambda_m^{(r)}}{2}\sum_\sigma \gamma_{\vec{R}_m^{(r)},\sigma,0}\gamma_{\vec{R}_m^{(r)},\sigma,1}\right)^2\right), \quad (24)$$

can be bounded in k ·k as follows:

$$\begin{aligned}\|H_{\mathrm{DF}} - \tilde{H}_{\mathrm{DF}}\| &\leq |\lambda_m^{(r)}| \sum_{n\neq m} |\lambda_n^{(r)}| + \frac{1}{2}|\lambda_m^{(r)}|^2 \quad (25)\\ &= |\lambda_m^{(r)}|\left(\|L^{(r)}\|_{\mathrm{SC}} - \frac{1}{2}|\lambda_m^{(r)}|\right)\\ &\leq \|L^{(r)}\|_{\mathrm{SC}}|\lambda_m^{(r)}|.\end{aligned}$$

In the coherent scheme, we truncate eigenvalues in the index set T so ϵ_{in}. In the incoherent scheme, we truncate such that

In both cases we may maximize the number of trun- $\|L^{(r)}\|_{\mathrm{SC}}|\lambda_m^{(r)}|$ cated eigenvalues by deleting those with the smallest value of first.

In the following, we truncate,

$$\sqrt{\textstyle\sum_{(r,m)\in\mathcal{T}}(\|L^{(r)}\|_{\mathrm{SC}}|\lambda_m^{(r)}|)^2} \leq \epsilon_{\mathrm{in}} \quad (26)$$

according to the sum-of-square procedure. While this approach does not rigorously bound the total error, we find that it better matches the error we observed for our benchmark systems, see Fig. 4, but still tends to significantly overestimate the actual error.

RESULTS

For the intermediates depicted in the catalytic cycle in Fig. 1, we carried out electronic energy calculations with various active orbital spaces for the analyses discussed below and density functional calculations that delivered the data presented in Fig. 2. For each of these key intermediates and transition states, we then evaluate the cost of performing quantum phase estimation to chemical accuracy, both for active spaces of 52–65 orbitals and larger ones, and then discuss runtimes and qubit requirements all summarized in the summary of progress. After that we discuss the new version of the reaction, the novel catalytic material (modified Ru), and the enhancement we made to the previous results obtained by the reaction.

Resource estimates

We now evaluate the cost of phase estimation to chemical accuracy for various structures in the carbon capture catalytic cycle of Section II. The active spaces of the molecules considered in this section are in the range of 52–65 orbitals, although we tabulate more results for 2–250 orbitals in the supplementary material. In addition, we also evaluate the scaling of cost with respect to the active space size N while keeping the number of atoms fixed and find a different scaling law of M ~ N2.5 for the number of eigenvectors compared to that of M ~ N log N when increasing the number of atoms. We find, as shown in Table I, that the gate cost for systems in the 52-orbital to the 65-orbital range is on the order of 1010

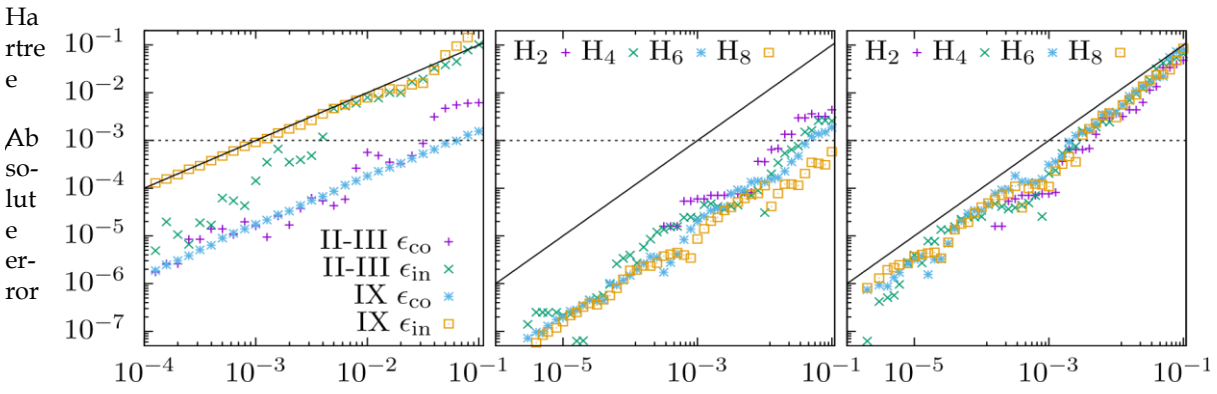

Figure 4. Empirical absolute error δ (in Hartree) of the ground-state electronic energy resulting from applying the two truncation schemes to the two-electron integrals of the Hamiltonian at various thresholds evaluated from DMRG-CI calculations.

Toffoli gates, using about 4000 qubits. The cost depends on the truncation threshold as plotted in Fig. 5. The numerically computed shift in energy at that threshold can exceed chemical accuracy, following Fig. 4, and should be interpreted as a most optimistic cost estimate. Therefore, we choose in = 1mHartree, which our numerical simulations indicate closely reflect chemical accuracy. Irrespective of the truncation scheme, we note that the logarithmic scaling with 1/ϵin means that the Toffoli costs vary by at most factor of five between these extremes. By varying the active space size between 2 and 250 orbitals for the different catalyst structures, we find in

Fig. 6 that the Toffoli cost of phase estimation scales with ~ N3.25. The exponent is a combination of two factors: Across all configurations of the catalytic cycle, the number of eigenvectors scales with M ~ N2.5, hence CW ~ √MN ~ N1.75, and the normalizing constant αDF ~ N1.5 Hartree. Our improvement largely stems from a normalizing factor αDF that is 33 to 120 times smaller as the number of terms in all approaches at this threshold are roughly equal. This trend also applies to the various carbon fixation catalyst structures that we consider when we perform a similar comparison but instead use the same incoherent truncation scheme for all examples at a more conservative error threshold of ϵin = 1mHartree.

Runtimes and qubit counts

We finally relate these gate count estimates to expected runtimes on future quantum computers. The exact runtime will, of course, depend on details of the system and error correction schemes. As a more realistic assumption for mid-term fault-tolerant quantum computers, we now expect that the physical gate times in current quantum computer architectures range from tens of nanoseconds for solid-state qubits to tens of microseconds for ion traps. Realizing fault tolerance by using quantum error correction with the surface code, will lead to logical gate times for a Toffoli gate of about 10μs to 10ms depending on the architecture. The lower estimate of 10μs means that 1010 Toffoli gates correspond to a runtime of 28 hours or about a day, while the upper estimate of 10ms would correspond to 8 days or about a week (Novel runtime result that exceeds our classical computers and the best previous quantum algorithms).

Fault-tolerant gates also have an overhead in the number of qubits, with hundreds to thousands of physical qubits needed per logical qubit, depending on the quality of the qubits. 4000 logical qubits will thus correspond to millions of physical qubits. This implies the need for a scalable quantum computer architecture, scaling to millions of qubits

Table 1. Number of Toffoli gates for estimating an energy level to an error of 1 mHartree using a truncation threshold of ϵ_{in}= 1mHartree for the largest active spaces of structures in the catalytic cycle considered here. Our approach allows for a trade-off between the number of logical qubits required and the Toffoli count.

Structure	Orbitals	Electrons	R	M	a_{DF} /Hartree	Using fewer qubits		Using fewer Toffolis	
						Qubits	Toffolis/10^{10}	Qubits	Toffolis/10^{10}
I	52	48	613	23566	177.3	3400	1.3	6900	1.1
II	62	70	734	33629	374.4	4200	3.6	8400	3.1
II-III	65	74	783	38122	416.0	4400	4.5	8900	3.7
V	60	68	670	29319	371.1	4100	3.3	8200	2.9
VIII	65	76	794	39088	425.7	4400	4.6	8900	3.8
VIII-IX	59	72	666	29286	384.4	4000	3.4	8000	2.9
IX	62	68	638	28945	396.6	4200	3.5	8400	3.1
XVIII	56	64	705	29594	293.5	3700	2.5	7400	2.1

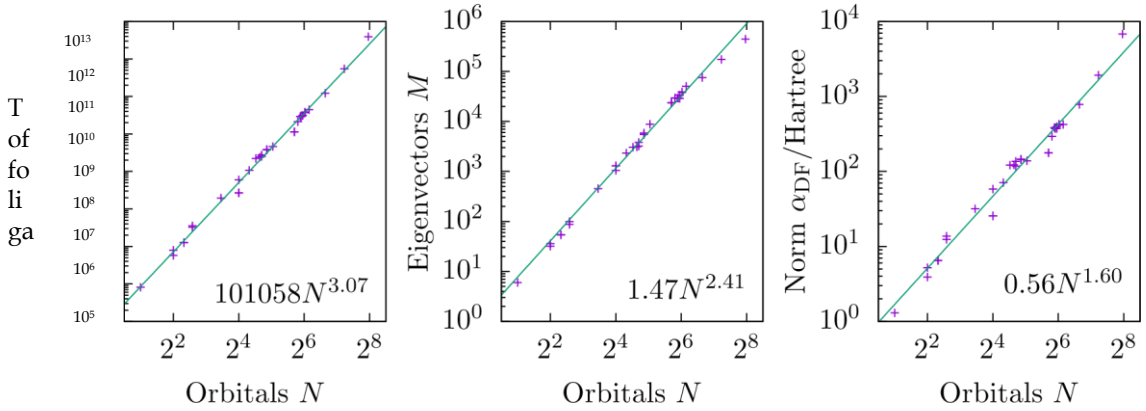

Figure 6. (Left) Scaling of minimized Toffoli cost across all configurations of the catalytic cycle with respect to active space size, for performing phase estimation to a precision of 1mHartree in the double-factorized representation. The fitted power-law curve has an exponent arising from the product $a_{DF}c_W \sim a_{DF}\sqrt{MN}/\Delta_E$ in Eqs. (1) and (19) (middle) where M is the number of eigenvectors and (right) the normalizing constant is a_{DF}.

Structure	Approach	a / Hartree	Terms	Qubits	Toffoli gates	Comments
VII	Qubitization H_{DF}	425.7	2.5×10^6	4600	4.6×10^{10}	ϵ_{in}=1mHartree
	Qubitization H	1.1×10^4	2.2×10^6	11000	9.3×10^{11}	ϵ_{in}=1mHartree
	Qubitization H_{CD}	4.2×10^4	1.3×10^6	5800	2.1×10^{12}	ϵ_{in}=1mHartree

Table 2. Our new double-factorization approach for with prior approaches based on Trotterization or qubitization using the unfactorized H or single-factorized H_{CD} Hamiltonian, and for the VIII structure in the catalytic cycle (N = 65) where all examples apply the incoherent truncation scheme with the same threshold of ϵ_{in}= 1mHartree.

State preparation

To determine the ground state energy using phase estimation, it is required to prepare a trial state $|\Psi trial\rangle$ which has a high overlap with the true ground state $|\Psi 0\rangle$ of the Hamiltonian H as discussed in Section IV. While the exact ground state is unknown, we used DMRG calculations to obtain an approximate ground state $|\tilde{\Psi}0\rangle$ for each of 15 our systems (see s for further details). An approximate configuration interaction wave function obtained by reconstruction from the corresponding matrix product state wave function optimized with DMRG served to provide an overlap with the trial state prepared on the quantum computer. Since the trial state is chosen to be HF determinant for this case, the overlap is given by the square of the coefficient in front of the Hartree-Fock determinant in the configuration interaction expansion, i.e., the one with the first N/2 orbitals occupied where N is the number of electrons. We found that there is a large overlap for all our systems, see Table IV. We expect this overlap to not shrink substantially with increasing precision of the approximate ground state obtained by DMRG and hence preparing the dominant single-determinant state is sufficient for the molecular structures considered in this work.

DFT AND ELECTRONIC ENERGIES CALCULATIONS

We chose seven key intermediates and transition states, therein labeled as complex structures II, II-III, V, VIII, VIII-IX, IX, and XVIII. These structures had been optimized with a combination of exchange-correlation density functional and basis set, and M06-L/def2-TZVP, PBE/def2-TZV, and PBE0/def2-TZVP energies were obtained which we used for the diagram in the main text. In this work, we continue to use the roman numerals as labels.

DFT CALCULATIONS

To be able to obtain relative reaction energies (see Table II), we optimized the reaction molecules CO2, H2, H2O, THF, and methane with Gaussian09, revision D.01 including density fitting and the Ultrafine keyword for the integration grid in accordance with the supporting information. For all other density functional theory (DFT) calculations reported herein we employed Turbomole, version 7.0.2. We then carried out PBE and PBE0 calculations in the def2-TZVP basis for each complex and the reaction molecules on the M06-L/def2-SVP structures.

To ensure that we obtained the correct global minima in the molecular orbital coefficient parameter space, we perturbed the α and β orbitals of the converged calculation with the orbital steering protocol. We repeated the respective calculation with the perturbed orbitals as starting orbitals to probe whether a solution of lower energy could be obtained.

We additionally optimized the structures with the PBE/def2-TZVP combination of density functional and basis set and carried out frequency calculations to ensure we had obtained the correct type of stationary points (no imaginary frequencies for intermediates).

M06-L energies for re-optimized molecules

For comparison, we report here the M06-L/def2-SVP electronic energies for the molecules which we re-optimized.

Table 3. M06-L/def2-SVP electronic energies for the optimized structures given in Hartree atomic units.

Compound	$E_{\mathrm{M06el-L}}$
H_2	-1.16721
H_2O	-76.35053
CO_2	-188.43534
CH4	-115.61382
THF	-232.24308

PBE and PBE0 electronic energies for fully optimized structures

The electronic energies of the PBE/def2-TZVP and PBE0/def2TZVP DFT calculations for the complexes and remaining compounds as well as the relative reaction energies of the complexes are collected in Table III and the ones of the re-optimized structures in Table IV. The relative reaction energies reported in these Tables were obtained in accordance with the supporting information and their formulaic calculation is given in Table II. We employ the double slash notation where the labels before the double slash denote the combination of exchange-correlation functional and basis set for the calculation whereas the exchange-density functional and basis set employed for the structure optimization is given after the double slash.

Table 4. Formulae for the calculation of relative reaction energies $\Delta E_{\mathrm{rel}}^{\mathrm{el}}$ for the complexes, where $E^{\mathrm{el}}(i)$ is the electronic energy of compound i computed with a certain combination of exchange correlation density functional and basis set.

Complex	Calculation of $\Delta E_{\mathrm{rel}}^{\mathrm{el}}$
I	0.0
II	$E^{\mathrm{el}}(\mathrm{II}) + E^{\mathrm{el}}(\mathrm{THF}) - E^{\mathrm{el}}(\mathrm{I}) - E^{\mathrm{el}}(\mathrm{CO_2})$
II-III	$E^{\mathrm{el}}(\mathrm{II\text{-}III}) + E^{\mathrm{el}}(\mathrm{THF}) - E^{\mathrm{el}}(\mathrm{I}) - E^{\mathrm{el}}(\mathrm{CO_2})$
V	$E^{\mathrm{el}}(\mathrm{V}) + E^{\mathrm{el}}(\mathrm{H_2}) - E^{\mathrm{el}}(\mathrm{I}) - E^{\mathrm{el}}(\mathrm{CO_2})$
VIII	$E^{\mathrm{el}}(\mathrm{VIII}) + E^{\mathrm{el}}(\mathrm{THF}) - E^{\mathrm{el}}(\mathrm{H_2}) - E^{\mathrm{el}}(\mathrm{I}) - E^{\mathrm{el}}(\mathrm{CO_2})$
VIII-IX	$E^{\mathrm{el}}(\mathrm{VIII\text{-}IX}) + E^{\mathrm{el}}(\mathrm{THF}) - E^{\mathrm{el}}(\mathrm{I}) - E^{\mathrm{el}}(\mathrm{CO_2})$
IX	$E^{\mathrm{el}}(\mathrm{IX}) + E^{\mathrm{el}}(\mathrm{THF}) - E^{\mathrm{el}}(\mathrm{I}) - E^{\mathrm{el}}(\mathrm{CO_2})$
XVIII	$E^{\mathrm{el}}(\mathrm{XVIII}) + E^{\mathrm{el}}(\mathrm{THF}) - 2 \times E^{\mathrm{el}}(\mathrm{H_2}) - E^{\mathrm{el}}(\mathrm{I}) - E^{\mathrm{el}}(\mathrm{CO_2})$

Table 5. PBE/def2-TZVP//M06-L/def2-SVP and PBE0/def2-TZVP//M06-L/def2-SVP energies E^{el} and relative reaction energies ΔE_{rel}^{el} given in Hartree atomic units.

Compound	Eel_{PBE}	$\Delta Eel_{rel,PBE}$	Eel_{PBE0}	$\Delta Eelrel,PBE0$
I	−2936.85035	0.0	−2937.09522	0.0
II	−2893.07375	−0.01824933	−2893.27797	0.01845670
II-III	−2893.06593	−0.02630769	−2893.26673	0.02969426
V	−3124.16485	−0.00142320	−3124.39830	−0.00479493
VIII	−2894.26852	−0.01061211	−2894.47992	−0.01533001
VIII-IX	−2893.06125	−0.03075055	−2893.26757	0.02886085
IX	−2893.08016	−0.01184458	−2893.28802	0.00840579
XVIII	−3051.28933	−0.00472200	−3051.53350	−0.01268354
H_2	−1.16590	–	−1.16817	–
H_2O	−76.37653	–	−76.37717	–
CO_2	−188.47898	–	−188.46644	–
CH4	−115.62907	–	−115.63697	–
THF	−232.23733	–	−232.26523	–

B. HF AND POST-HF CALCULATIONS

We obtained Hartree-Fock (HF) and Complete Active Space Self-Consistent Field (CASSCF) molecular orbitals (MOs) in an ANO-RCC-VTZP atomic orbital (AO) basis for the light elements and ANO-RCC-VQZP for Ruthenium with OpenMolcas. We employed a Cholesky Decomposition (CD) of the many-electron repulsion integrals and generated two sets of integrals with decomposition thresholds of 10−4 and 10−8, respectively (note that this decomposition which occurs during the quantum chemical calculations is separate from a later truncation of the many-electron integrals in the context of the quantum computing algorithms). The choices for the molecular and atomic orbital bases in this study are summarized in Table V.

For quantitative results, it is necessary to employ a larger AO basis, we performed exploratory calculations of the ANO-RCCMB, the ANO-RCC-VTZP for light elements and ANO-RCC-VQZP for Ruthenium, which we will term the full atomic orbital basis (fb). Table VI lists the number of many-electron basis functions resulting from the choice of these bases for each complex.

Table 6. PBE/def2-TZVP//PBE/def2-TZVP electronic energies $E^{el,opt}$ after structure optimization and corresponding relative reaction energies $\Delta E_{rel}^{el,opt}$ given in Hartree atomic units.

Compound	$E_{PBE}^{el,opt}$
I	− 2936 .85482
II	− 2893 .07854
II-III	− 2893 .06962
V	− 3124 .17151
VIII	− 2894 .27315
VIII-IX	− 2893 .06751
IX	− 2893 .08609
XVIII	− 3051 .29506
H_2	− 1.16591
H_2O	− 76.37676
CO_2	− 188 .47928
CH	− 115 .62962
THF	− 232 .23812

The AOs are generally labeled by the type of method with which they have been obtained, i.e., HF and CASSCF. When necessary, the active space employed in the CASSCF calculation is given explicitly through the notation (N,L) (e.g., CAS(6,6)SCF), where N is the number of electrons and L the number of orbitals in the active space.

Table 7. Overview of different types of many-electron basis sets employed in this study.

Basis	Basis set	Comment
Atomic orbitals	ANO-RCC-MB ANO-RCC-VTZP for Light elements ANO-RCC-VQZP for Ruthenium	Abbreviation: fb
Molecular orbitals	HF	
	CAS(*N*,*L*)SCF	(*N*,*L*): Active space of *N* electrons in *L* orbitals

Table 8. Number of many-electron basis functions for each complex for the full atomic orbital basis 'fb', as described in the text and in Table V.

Complex	Fb
I	2286
II	2114
II-III	2114
V	2348
VIII	2142
VIII-IX	2114
IX	2114
XVIII	2374

HF, CASSCF, and DMRG-CI electronic energies

The CASSCF molecular orbitals from calculations with a Cholesky Decomposition threshold of the many-electron integrals of 10−4 were obtained in the following manner: HF orbitals in the ANO-RCC-FB atomic orbital basis were split-localized with the Pipek-Mezey method. From these localized orbitals, we selected the orbitals corresponding to the 4d orbitals of Ruthenium, the 2p and 2s orbitals of Oxygen and Carbon atoms (i.e. the bonding and antibonding π orbitals of carbon dioxide and derivatives), the bonding and antibonding σ orbitals of H2 as well as the s-orbitals of Hydrogen atoms to evaluate their orbital entanglement and pair-orbital mutual information in an approximate Density Matrix Renormalization Group-Configuration Interaction (DMRG-CI) calculation with maximum bond order m = 800 and n = 5 with the QCMaquis program. We selected the orbitals corresponding to a threshold in autoCAS as the active space for a subsequent CASSCF calculation. We repeated the approximate DMRG calculation on these new CASSCF orbitals and chose those orbitals selected by the autoCAS program as the final active orbital space. We then expanded these orbitals to the full atomic orbital basis with the EXPBAS module of OpenMolcas and re-optimized them in a final CASSCF calculation. For the calculations involving a Cholesky Decomposition threshold of 10−8, we started the CASSCF calculations directly from the corresponding CASSCF orbital file of the calculations with a threshold of 10−4 to save computational resources.

Complex	$CD_{threshold}$	HF_{Energy}	CAS(N_c,L_c)SCF_{Energy}	(N_c,L_c)	DMRG(N_d,L_d)CI_{Energy}	(N_d,L_d)
I	10^{-4}	-7361.315677	-7361.357885	(4,5)	-7361.461381	(48,52)
I	10^{-8}	—	-7361.360402	(4,5)	—	—
II	10^{-4}	-7317.956458	-7318.035225	(8,6)	-7318.123548	(70,62)
II	10^{-8}	—	-7318.037547	(8,6)	—	—
II-III	10^{-4}	-7317.931739	-7317.999907	(8,6)	-7318.099062	(74,65)
II-III	10^{-8}	—	-7318.002150	(8,6)	—	—
V	10^{-4}	-7548.043678	-7548.214683	(12,11)	-7548.296446	(68,60)
V	10^{-8}	—	-7548.217104	(12,11)	—	—
VIII	10^{-4}	-7319.116649	-7319.140267	(2,2)	-7319.234732	(76,65)
VIII	10^{-8}	—	-7319.142596	(2,2)	—	—
VIII-IX	10^{-4}	-7317.937509	-7317.971210	(4,4)	-7318.066197	(72,59)
VIII-IX	10^{-8}	—	-7317.973426	(4,4)	—	—
IX	10^{-4}	-7317.970467	-7318.209829	(16,16)	-7318.303045	(68,62)
IX	10^{-8}	—	-7318.212256	(16,16)	—	—
XVIII	10^{-4}	-7475.314796	-7475.367378	(4,4)	-7475.439228	(64,65)
XVIII	10^{-8}	—	-7475.369956	(4,4)	—	—

Table 9. HF, CAS(N_c,L_c)SCF, and DMRG(N_d,L_d)CI electronic energies in Hartree for the complexes in the full atomic orbital basis obtained with different values of the Cholesky Decomposition threshold. (N_c,L_c) denotes the active space of the CASSCF calculations and (N_d,L_d) the one of the DMRG-CI calculations. For these, N_c and N_d refer to the number of electrons and L_c and L_d to the number of orbitals, respectively.

The many-electron integrals of a subset of these orbitals then served as parameters for the Coulomb Hamiltonian, for which the quantum-algorithm resource estimates were obtained. The general procedure for the selection of these active spaces is identified whereas the molecular orbitals resulting from this selection for each complex are reproduced.

For each structure, we additionally carried out DMRG-Configuration-Interaction (CI) calculations of the orbitals corresponding to the integral file with the largest active space to gain qualitative information about the electronic structure. These calculations were performed with a number of sweeps n = 10 and a maximum bond dimension m = 1000 and Fiedler ordering and on the integral files with a CD truncation threshold of 10−4. From the matrix product states generated in this way, we obtained the largest CI coefficient through a reconstruction of an approximate CI wave function expansion through the sampling-reconstruction algorithm. For the latter algorithm, we employed a CI-threshold of 10−6 and a CI completeness measure of 10−6. We confirmed that the choice of the CD threshold does not have a substantial influence on these overlap values as shown in Table VIII for complex IX (which features the smallest overlap of all structures).

Table 10. Comparison of the overlap $|D\tilde{\psi}|_0 |\psi\rangle_{\text{trialE}}|^2$ of the dominant single-determinant state $|\psi_{\text{trial}}\rangle$ with the approximate ground state $\tilde{\psi}_0$ obtained with DMRG-CI for complex IX. The active space is given by the number of electrons N and orbitals L. The maximum bond order dimension m and the number of sweeps n of the parent DMRG-CI calculation is given as well.

Catalyst structure	Active space (N, L)	CD threshold	m	n	Overlap
IX	(68,62)	10^{-4}			
IX	(68,62)	10^{-8}			
IX	(68,62)	10^{-4}			

The energies of the HF, CASSCF, and DMRG-CI calculations are reported in Table VII. We studied the effect of the accuracy of the wave function on the overlap calculated after applying the reconstruction algorithm by comparing with DMRG results obtained for bond dimensions and energetical orderings of the orbitals on the lattices (we refrain from reporting the explicit total energies of these calculations in order not to confuse the reader with less converged energy data). For our catalyst structures, as expected, Fiedler ordering of the orbitals turned out to improve the energy by about 0.061 mHartree to 0.1 Hartree (purpose achieved).

SUMMARY OF PROGRESS

In this section, we will exhibit our progress in results we were the first to accomplish in quantum computing and computational chemistry. Firstly, after a long journey of research and hard work that last for two years, we have proudly achieved novel results that surpass the best previous results conducted by prior quantum algorithms and classical computers:

- We were the first to solve the challenge of the electronic energies' calculation. We have successfully expressed and diagonalized the full many-electron Hamiltonian that was considered a barrier for quantum computing to use its computational power for simulating large systems and high numbers of correlated orbitals and electrons. Our diagonalization process has taken about 28 orbitals to be feasible and this number of correlated orbitals in full many-electron configuration is considered as a record calculation among all the trials to reach an efficient result that can reveal new discoveries about a chemical reaction or even an element to develop.

- We were the first to extract practical results from using the classical methods of computational chemistry that accompany quantum algorithms in order to present a complete solution, as Multi-configurational self-consistent field (CASSCF), Density matrix renormalization group (DMRG), and full configuration interaction quantum Monte Carlo (FCIQMC) in (fig.3), we also use DMRG as the accompanied method with the quantum phase estimation algorithm to assess the ground state energy level of reactants, products, and all forms of the catalyst during the reaction (as shown in the results section).

- We were the first to reach a new record runtime of simulating a complete chemical system on a fault-tolerant quantum computer (week - 8 days) while the last record [6] was about 4 weeks.

- We also provide the most accurate results have been ever obtained of the electronic energies of the Ru catalytic reaction using our new algorithm called SYCAMORE (Sycamore is a combination of all the quantum algorithms and classical methods that we use in our work to calculate electronic energies) as shown in Table. 9.

After accomplishing these unprecedented results and acquiring our purposes, the results gave us huge knowledge about the chemical properties of the reaction components that opens the door to develop the reaction mechanism, modify the catalytic material, and thus enhance carbon removal results of the reaction. We will take about the new discoveries, modifications, improvements, that make our specified reaction a promising solution for carbon removal, in the next sections.

Algorithmic Advancement & Results Enhancement

In this section we will discuss the discoveries, the way that maximizes the efficiency of reaction mechanisms and components, and how we can run them in the best circumstances. After that we will deliberate the novel catalytic material that we created and the enhanced results of the process that reached the Mt/y after being insufficient to remove carbon.

After an intensive study of the catalyst and catalytic reaction, in addition to the algorithmic advance of the reaction simulation that divulges a lot of findings such as:

- The chemical properties of Ruthenium catalyst make it be more efficient if it works as a dual function material with intimate contact with alkaline component, we have studied the possible candidates and found that the sodium carbonate (Na2CO3) in the best contender. In our experiments, we observed that Ru achieves the highest result of CO2 capture and methanation in the case of working with Na2CO3. We will validate all the experimental results in the following section.

- During the process of reaction development, we found that the catalytic material presents such effective carbon dioxide adsorption, when it works on a metal oxide high surface area carrier as (Al2O3) because it provides a series of equilibrium shifts enhancing CO2 adsorption in synthesis gas reactions, forming a closed loop of CO2 adsorption and fixation. Al2O3 was evaluated among other entrants as (ZrO2), and it exhibited excessive results as component of the catalytic material.

- From the studies conducted on Ruthenium, we observed that Ru has a unique feature of Ru/RuOx is its redox chemistry of rapid and reversible transformation between its oxide and metallic states. Reasonably, we assumed that increasing the partial pressure of H_2 would have the same effect by maintaining the Ru in the metallic and active state while increasing the extent of carbonate hydrogenation. This was demonstrated in Figure 9 where 10% H_2/Ar dramatically increased the amount of methane produced (60 kg-mol) compared to 5% H_2/Ar (22 kg-mol). This also points to the importance of the redox chemistry of Ru/RuO_x.

In the following sections we will describe the catalytic material, establish the experiment, show the results of CO_2 removal and fixation, and compare it with the latest version of catalytic material and the reaction happened in the same conditions to show how we have progressed with our quantum algorithm in the area of climate change and carbon removal technologies.

Problem to be solved

Coal-fired power plants emit significant amounts of CO_2 into the atmosphere and carbon emission taxes are starting to be implemented in industrially developed countries. In order to reduce environmental pollution and avoid emission taxes, we have chosen a strategy: (capturing and sequestering the CO_2). Using CO_2 as a carbon source, instead of emitting it as a waste, is a promising and attractive solution. In this approach, a worthless compound as CO_2, can be converted into commercial chemicals or combustibles.

The valorization of CO_2 is challenging since the transformation of carbon dioxide into chemical products makes sense only if using renewable energies and renewable raw materials. The hydrogenation of CO_2 leads to a large variety of products such as methane, methanol, carbon monoxide and formic acid. Among the different conversion solutions, the methanation of CO_2 is the most favored reaction by the thermodynamics and energy demand. Carbon dioxide, captured from the flue gas of industrial processes, can react catalytically with renewable H_2 to produce synthetic natural gas (SNG), by the reaction of Sabatier:

$$CO_2+4H_2 \leftrightarrows CH_4+H_2O \quad (\Delta H=-164\ kJ/mol) \qquad (1)$$

We are now representing a work-in-progress combining a series of adsorption and catalytic reactions for converting adsorbed CO2 emitted from power plant oxygen-containing flue gas where the redox property of Ru/RuO_x is critical for successful use. The material used for this process is composed of a nano-dispersed alkaline component (Na2CO3) in intimate contact with Ru on a high surface area carrier (Al2O3), referred to as a Dual Function Material (DFM). These materials allow CO_2 storage and direct conversion to methane without the need for energy intensive thermal CO_2 purification processes. It adsorbs CO2 on its alkaline component and catalytically converts it to

synthetic natural gas (CH4) in the subsequent step over the Ru catalyst approaching a closed loop for carbon fixation. Alkaline carbonates have been reported to be efficient for CO2 adsorbents.

In this approach, when the catalyst is saturated with CO_2 and H_2 is injected, a spillover phenomenon occurs that leads the chemisorbed CO_2 to the catalytic centers of the noble metal where the methanation occurs. This fact means that the energy requirement of the process is limited to obtaining H_2, and therefore, the CO_2 capture process, conversion to CH_4 and subsequent use of the fuel approximates a CO_2 neutral cycle, with no net emissions from this gas to the atmosphere. This requires obtaining hydrogen from a renewable energy source. Other configurations have been studied later on for the combined CO_2 capture and catalytic conversion to methane. Veselovskaya et al. studied the possibility of performing the capture and methanation in physically separated stages. The advantage of this configuration is the possibility to optimize the two processes of capture and methanation, for example in terms of temperature and pressure. Later studies evaluated the feasibility of performing the capture and methanation process in the same physical unit using two different solids. The advantage of this configuration is the lower investment cost (only one reactor for both processes). Also, the preparation of both types of solids can be optimized separately, in a search for high adsorption or methanation performance. Even so, a unique reactor configuration using DFMs obtains better results due to the close proximity between the basic storage sites for CO_2 adsorption and metallic sites for hydrogenation, both impregnated onto the same support. Both the CO_2 capture process and the CH_4 conversion process can operate at 300–400 °C, a temperature that can be supplied by heat recovered from the emission stream, without the need of external heat input. The DFM is placed in two parallel reactors which operate alternating CO_2 storage and hydrogenation cycles. In a typical implementation of this material, the methane produced is dried and compressed, and recycled to the inlet of the power plant or integrated into the natural gas grid, ideally closing the carbon cycle as shown in fig. 7. Thus, this material provides an additional source of sites for CO2 capture by carbonate reformation, yielding an increase in carbon capture and subsequent methane production.

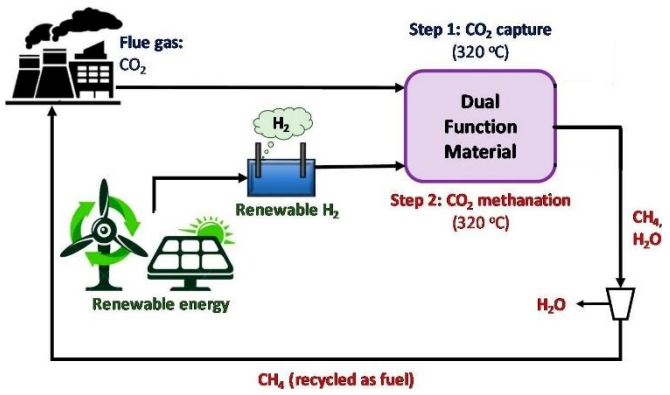

Fig. 7: Schematic summarizing the dual-function material (DFM) carbon removal cycle.

Our team has been a pioneer in the development of DFMs for the CO_2 capture and hydrogenation to CH_4 after the advancement of quantum computation. In the current paper, we are presenting an extensive study on the properties of Ru-Na_2CO_3/Al_2O_3 catalysts with increasing adsorbent loadings, to demonstrate
an efficient solution for carbon removal challenge. We also analyze the temporal evolution of reactants and
products, i.e., CO_2, CO, H_2O and CH_4 during the CO_2 sequestration and hydrogenation cycles.
Based on these results, we propose a complete reaction mechanism validated on experimental evidence. Differences in the catalytic performance towards the CO_2 adsorption and hydrogenation at different temperatures (280–400 °C) are correlated with the physico-chemical properties of the prepared catalysts.

EXPERIMENTAL

2. Catalyst preparation

All samples were prepared by wetness impregnation. First, appropriated amount of ruthenium (III) nitrosyl nitrate $Ru(NO)(NO_3)_2$ and Na_2CO_3 was impregnated over a high surface area γ-Al_2O_3. The impregnated powder was dried at 120 °C overnight and then calcined in air at 400 °C to decompose the precursor salt. Afterwards, Ru was impregnated over xNa_2CO_3/Al_2O_3 (x = 5, 10 and 15%). This impregnation sequence, i.e., the adsorbent and then the noble metal, has been reported to achieve better catalytic performance and was also verified in this work, as reported in the supplementary material (Figure S1). After drying at 120 °C, the samples were stabilized by calcining again at 400 °C in air for 4 h.

2. X Ray Diffraction (XRD)

X-ray diffraction patterns were obtained in a *Philips PW1710* diffractometer. The samples were finely ground and were subjected to Cu Kα radiation in a continuous scan mode from 5° to 70° 2θ with 0.02 per second sampling interval. *PANalytical X'pert HighScore* and *Winplotr* profile fitting software were used for data treatment.

2. N_2 adsorption-desorption

The N_2 adsorption-desorption analysis were carried out at the nitrogen boiling temperature (−196°C) using an automated gas adsorption analyzer (*TriStar II, Micromeritics*). The samples were purged with nitrogen for 10 h at 300 °C using *SmartPrep degas system* (*Micromeritics*).

H_2 chemisorption

Ruthenium dispersion was determined using the H_2 chemisorption method in a *Micromeritics ASAP 2020* equipment. The catalyst (0.35 g) was first outgassed at 300 °C for 60 min and reduced in 50 ml min^{-1} of 5% H_2/Ar at 350 °C during 2 h. Then, the sample was further outgassed at 360 °C for 90 min. Finally, H_2 was dossed for obtaining the adsorption isotherm at 35 °C. Before repeating the adsorption isotherm, the sample was again outgassed for 60 min, and the difference between first and second isotherms was related with the amount of H_2 chemisorbed on the catalyst surface.

Transmission electron microscopy (TEM)

The morphology of the samples was analysed by transmission electron microscopy (TEM) in a *Philips CM200* transmission electron microscope with a LaB6 filament as the source of electrons operated at 200 kV. The samples were dispersed in absolute ethanol ultrasonically, and the solutions were then dropped on copper grids coated with lacey carbon film.

samples were heated from RT to 350 °C at 10 °C min^{-1} in a 5% H_2/Ar stream with a total flowrate of 50 ml min^{-1} until a complete reduction of the samples before the experiment. Subsequently, the samples were exposed to a gas stream composed of 5% CO_2/He at 30 ml min^{-1} for 1 h at RT to saturate the catalyst with CO_2. Then, the samples were exposed to Helium for 90 min to remove the physically adsorbed CO_2. Finally, the samples were heated from RT to 900 °C at 10 °C min^{-1} and the CO_2 released was measured by mass spectrometry (*OMNI StarTM*).

Temperature programmed surface reaction (TPSR)

The TPSR experiments were carried out in a quartz tube reactor placed in a horizontal furnace. The sample (0.3 g) was pretreated under 5% H_2/Ar at 400 °C until the complete reduction of ruthenium, and then, the sample was cooled down to 50 °C. Subsequently, the samples were exposed to a gas stream composed of 28% CO_2/Ar with a flowrate of 700 ml min^{-1} for 20 min at 50 °C to saturate the catalyst with CO_2. Afterwards, the

Table 11: Nomenclature, adsorbent loading and textural properties of the prepared catalysts and the reference materials.

1) Sample	1) Nomenclature	1) Adsorbent wt.%	1) SBET, m2/g	1) d_p, Å	1) V_p, cm^3/g
1) γ-Al_2O_3	2) Al2O3	2) –	2) 217.3	2) 107.5	2) 0.60
1) 4% Ru/Al_2O_3	3) Ru/Al_2O_3	3) –	3) 198.6	3) 103.3	3) 0.53
1) 10% Na_2CO_3/Al_2O_3	4) 10Na_2CO_3/Al_2O_3	4) 5.8% Na_2O / 10% Na_2CO_3 / 15.8% $NaHCO_3$	4) 184.5	4) 109.0	4) 0.52
1) 4% Ru 5% Na_2CO_3/Al_2O_3	5) Ru5Na_2CO_3	5) 2.9% Na_2O / 5% Na_2CO_3 / 7.9% $NaHCO_3$	5) 194.2	5) 101.1	5) 0.52
1) 4% Ru 10% Na_2CO_3/Al_2O_3	6) Ru10Na_2CO_3	6) 5.8% Na_2O / 10% Na_2CO_3 / 15.8% $NaHCO_3$	6) 164.7	6) 103.5	6) 0.45
1) 4% Ru 15% Na_2CO_3/Al_2O_3	7) Ru15Na_2CO_3	7) 8.8% Na_2O / 15% Na_2CO_3 / 23.8% $NaHCO_3$	7) 119.6	7) 116.6	7) 0.36

Temperature-programmed reduction (H_2-TPR)

The reducibility of the samples was investigated by temperature programmed reduction (H_2-TPR) in a Micromeritics AutoChem II equipment. The quartz tube reactor was loaded with 0.1 g of sample, which was pretreated with 5% O_2/He at 350 °C and then cooled down to 35 °C. Afterwards, samples were heated from RT to 950 °C at of 10 °C min^{-1} in 5% H_2/Ar stream with a flowrate of 30 ml min^{-1}. Water generated during samples reduction was removed using a cold trap before the gas was analyzed which a TCD detector. For some experiments, the effluent gas was also analyzed in a MultiGas 2030 FT-IR analyzer to quantify the formation of products during the reduction.

Temperature-programmed desorption (CO_2-TPD)

The CO_2-TPD experiments were carried out in a *Micromeritics AutoChem II* equipment. The samples (0.1 g) were pretreated at 400 °C under He and then cooled down to 35 °C. Thereafter, samples were heated from 50 to 600 °C at 10 °C min^{-1} in a 5% H_2/Ar mixture with a flowrate of 700 ml min^{-1}. The MultiGas 2030 FT-IR analyzer was used to quantify the formation of products during the reduction in the reactor effluent gas.

Reactor testing

The catalytic activity of the samples was evaluated in a vertical stainless steel tubular reactor loaded with 1 g of pelletized (0.3-0.5 mm) catalyst. Prior to the analysis, the sample was reduced under 10% H_2/ Ar at 350 °C for 45 min. During the storage step, 1.4% CO_2/Ar or 11% CO_2/Ar was fed for 1 min, followed by a purge with Ar for 2 min to remove the weakly adsorbed CO_2. Then, during the hydrogenation step, 10% H_2/Ar was fed for 2 min, followed by a purge with Ar for 1 min before starting again the storage step. Throughout the experiment, the total flow rate was 1200 ml min^{-1}, which corresponds to a GHSV of 45.000 h^{-1}. The experiments were carried out in the temperature range between 280 and 400 °C.

The composition of the exhaust gas was continuously analyzed using the MultiGas 2030 FT-IR analyzer for the quantitative analysis of CO_2, CH_4, CO and H_2O. The CO_2 adsorption capacity during the storage step was calculated with Eq. (2), whereas the amount of CH_4, CO and H_2O produced during the hydrogenation step was calculated with Eq. (3),(4) and (5), respectively. Definitive catalytic parameters were calculated as average values of three consecutive cycles.

$$\text{Stored } CO_2\ (\mu\text{mol g}^{-1}) = \int_0^{t_\omega} [F_{CO_2}^{in} - F_{CO_2}^{out}(t)]dt \quad (1)$$

$$CH_4\ (\mu\text{mol g}^{-1}) = \int_0^{t_n} F_{CH_4}^{out}(t)dt \quad (3)$$

$$CO\ (\mu\text{mol g}^{-1}) = \int_0^{t_n} F_{CO}^{out}(t)dt \quad (4)$$

$$H_2O\ (\mu\text{mol g}^{-1}) = \int_0^{t_n} F_{H_2O}^{out}(t)dt \quad (5)$$

RESULTS AND DISCUSSION

Structural properties of the prepared catalysts

The nomenclature and structural properties of the prepared catalysts, together with the corresponding reference materials, are summarized in Table 11. The adsorbent loading has been expressed as a function of the chemical nature, i.e., oxide (Na_2O), carbonate (Na_2CO_3) and bicarbonate in the case of sodium ($NaHCO_3$). The reference material for the adsorption of CO_2 has been considered Na_2CO_3. The specific surface area of the γ-Al_2O_3 was found to be 217 $m^2\ g^{-1}$. The incorporation of the adsorbent, i.e., 10%Na_2CO_3/Al_2O_3, significantly decreased the specific surface area to 184 $m^2\ g^{-1}$, attributed to the partial blocking of the pores of the support. In the same line, the incorporation of ruthenium to the alumina, i.e. 4%Ru/Al_2O_3, also produced a decrease in the exposed surface area but in a minor extent (199 $m^2\ g^{-1}$). As expected, when the adsorbent and the noble metal are successively impregnated over the alumina support, the specific surface area is further penalized. The adsorbent content has a notable impact in the specific surface area. The higher the adsorbent loading, the lower the surface area is. Specifically, sodium carbonate penalizes in a greater extent the exposed surface area 120 $m^2\ g^{-1}$, for an adsorbent content of 15%. Similar conclusions can be extracted from the evolution of the total pore volume. No significant changes can be observed in the average pore diameter after the incorporation of the noble metal and the adsorbent.

Fig. 8 shows the most representative XRD profiles of the synthesized samples. All the samples presented some diffraction peaks attributed to one or more crystalline structures. Wide diffraction peaks with low intensity, characteristic of γ-Al_2O_3, are observable in all samples. The XRD patterns of 10%Na_2CO_3/Al_2O_3 samples slight differ from that of bare alumina, which means that the adsorbents do not form a crystalline structure probably because they are well dispersed over the alumina support. Even for the samples containing the highest adsorbent loading (15%), diffraction peaks belonging to Na_2CO_3 are not detected (Figure S2). These results agree with those obtained which did not appreciate peaks of Na_2CO_3 up to a 25 wt.%. On the contrary, three intense peaks belonging to RuO_2 (▲) are distinguished for all the samples containing ruthenium.

Effect of H_2 Partial Pressure on CO_2 Hydrogenation and Ru-O_x Reduction

It is reasonable to assume that increasing the partial pressure of H_2 would have the same effect by maintaining the Ru in the metallic and active state while increasing the extent of carbonate hydrogenation. This was demonstrated in Figure 14 where 10% H_2/Ar dramatically increased the amount of methane produced by (60 kg-mol) compared to 5% H_2/Ar (22 kg-mol). This also points to the importance of the redox chemistry of Ru/RuO_x.

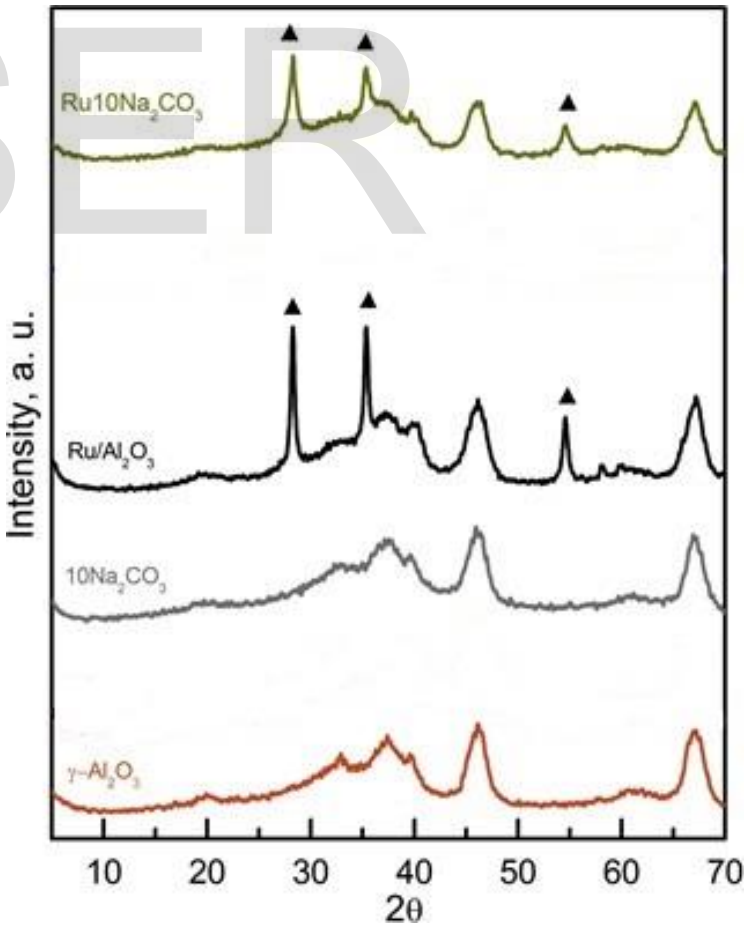

Fig. 8. XRD diffraction patterns for Ru10Na2CO3 together with reference samples. Diffraction peaks belonging to RuO2 are identified with solid triangles (▲).

Ru dispersion

Ruthenium dispersion has been estimated by H_2-chemisorption considering a chemisorption stoichiometry of H/Ru = 1, resulting in the values collected in Table 12. Modest ruthenium dispersion is obtained for all the prepared catalysts.

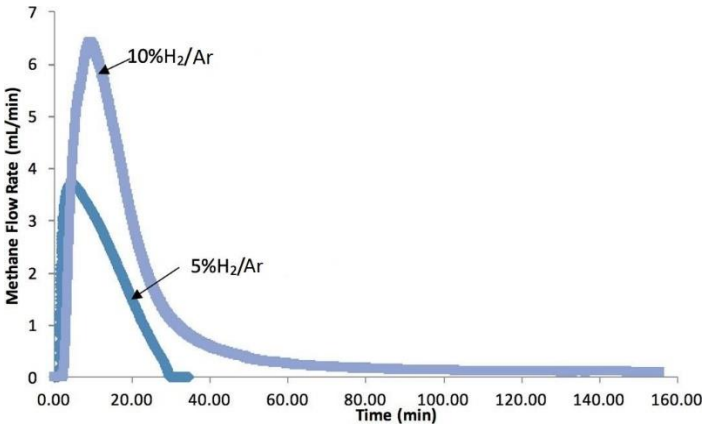

Figure 9. Methane production comparison of 5% H2/Ar and 10% H2/ Ar. The test was operated using 10 grams of 5% Ru, 10% Na2CO3/Al2O3 pellets. The operational conditions were at 320 ◦C, 300 mL/min of 7.5% CO2/Ar for CO2 adsorption. The volume of methane produced are shown.

Table 12: Ru dispersion estimated by H_2 chemisorption, Ru particle size derived from the dispersion value and from TEM micrographs.

Sample	Ru disp, %	d_c (chem), nm	d_c (TEM), nm
$Ru5Na_2CO_3$	11.6	11.5	9.7
$Ru10Na_2CO_3$	18.7	7.1	8.2
$Ru15Na_2CO_3$	19.3	6.9	7.7

For the catalysts containing Na_2CO_3 as adsorbent, a maximum Ru dispersion of 19% is obtained for the sample with the highest loading of adsorbent, i.e., $4\%Ru15\%Na_2CO_3/Al_2O_3$. Ru dispersion is reduced to 18% and 12% for Na_2CO_3 loadings of 10 wt.% and 5 wt.%, respectively. Thus, although increasing loadings of Na_2CO_3 penalized the exposed surface area, the dispersion of Ru was favored. Transmission Electron Microscopy (TEM) was also employed to determine the size of Ru particles (Fig. 10). The darker spherical areas in the micrograph correspond to Ru, which was confirmed by EDX. The average particle size the Ru particles estimated by measuring the size of at least 100 particles and results are collected in Table 12. The particle sizes measured by TEM is follo-w same trend than particle sizes determined by H_2 chemisorption. The particle size was reduced with the adsorbent loading and Ru aggregates were not detected. Thus, TEM images confirmed that Na_2CO_3 loading serves as a promoter.

Temperature-programmed experiments (CO_2-TPD and H_2 TPR)

The basicity of the prepared samples was determined by CO_2-TPD (Fig. 11). The samples with a low content of adsorbent (5 wt.%) illustrated a single CO_2 desorption peak at low temperature. On the contrary, the samples with a higher adsorbent loading (10 wt.% and 15 wt.%), presented two CO_2 desorption peaks at low and high temperature. The low temperature desorption peak is assigned to weakly or physically adsorbed CO_2 on the catalyst surface. The high temperature desorption peak is assigned to strongly adsorbed CO_2 forming stable carbonates (CO_3^{2-}) or bicarbonates (HCO_3-).

As shown in Table 13, the strong basicity was remarkably increased to (750 kg-mol CO_2 kg^{-1}). The low temperature desorption peak was centered at 120 °C irrespective of the adsorbent loading. However, the high temperature desorption peak was progressively moved to higher temperatures, i.e. 520, 630 and 680 °C, for increasing adsorbent loadings of 5, 10 and 15 wt.%, respectively. This fact indicates that the strength of the strong basicity progressively increases
probably due to the formation of small Na_2CO_3 aggregates that adsorb CO_2 to form a stable phase.
Similar conclusions can be extracted from Table 13 in the case of Na_2CO_3. The weak basicity is predominant in the case of low adsorbent loadings and strong basicity is promoted for higher loadings. However, some differences are also detected. First, the contribution of the weak basicity is notably higher for Na_2CO_3. Note that even for the highest adsorbent loading the weak basicity is predominant. Second, the strength of the strong basicity is lower for Na_2CO_3. The high temperature CO_2 desorption peak is centered at somewhat lower temperatures, i.e. 480, 560 and 640 °C, revealing that carbonates are so stable.
As metallic Ru and alumina are able to participate in the storage of CO_2 a specific experiment was carried out with the $4\%Ru/Al_2O_3$ sample. It was determined that this sample was able to store and then desorb 110 kg-mol CO_2 kg^{-1}. Consequently, in order to calculate accurately the amount of CO_2 desorbed specifically from the adsorbent, the amount of CO_2 desorbed from the $4\%Ru/Al_2O_3$ sample was subtracted. Following this procedure, the ratio of desorbed moles of CO_2 per mol of adsorbent was calculated and is collected in Table 13.

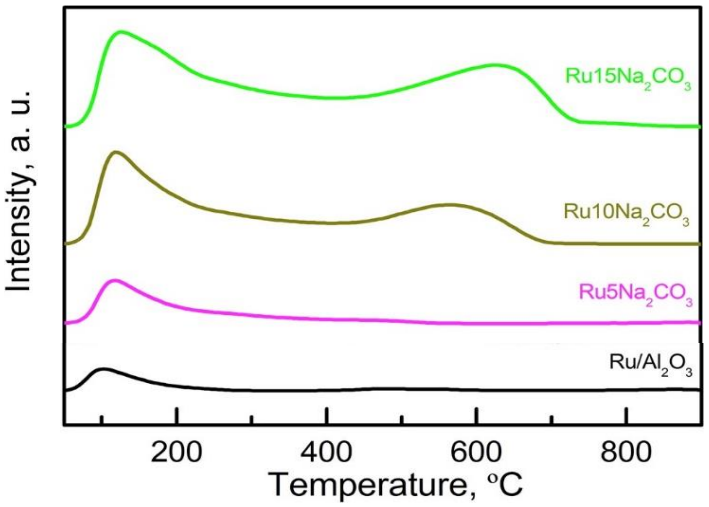

Fig. 10. CO2-TPD patterns for pre-reduced Ru-Na2CO3/Al2O3 samples with different adsorbent contents, i.e. 5, 10 and 15 wt.%. Ru/Al2O3 sample is also included as

Table 13. Weak, strong and total basicity of the prepared samples. The utilization of the adsorbent is also included in the last column.

1) Sample	1) Weak basicity, kg-mol $CO_2\,kg^{-1}$	1) Strong basicity, kg-mol $CO_2\,kg^{-1}$
1) $Ru5Na_2CO_3$	2) 196	2) 29
1) $Ru10Na_2CO_3$	3) 310	3) 244
1) $Ru15Na_2CO_3$	4) 520	4) 300
1) Ru/Al_2O_3	5) 86	5) 24

*Weak basicity is determined as the moles of CO_2 desorbed below 400 °C.

* Strong basicity is determined as the moles of CO_2 desorbed above 400 °C. * Adsorbent utilization is expressed as the moles of CO_2 desorbed per mol of adsorbent

Considering the decomposition reactions of sodium carbonate ($Na_2CO_3 \rightarrow Na_2O + CO_2$) one would expect 1 mol of CO_2 desorbed per mol of adsorbent if the adsorbent was completely carbonated before the CO_2-TPD. As can be observed in Table 13, the ratio was situated below 1 for all the samples, indicating that the utilization of the adsorbent was not total.

The utilization of the adsorbent is 0.32 for an adsorbent loading of 5 wt.%. However, the (CO_2/Na_2CO_3) ratio increases to 0.73 and 0.72 for Na_2CO_3 loadings of 10 and 15 wt.%, respectively. This higher utilization of the adsorbent could be due to a better dispersion of Na_2CO_3 or to the ability of sodium carbonate to form sodium bicarbonate. Indeed, the decomposition of sodium bicarbonate to sodium carbonate ($2NaHCO_3 \rightarrow Na_2CO_3 + H_2O + CO_2$) and the subsequent decomposition of sodium carbonate to sodium oxide ($Na_2CO_3 \rightarrow Na_2O + CO_2$) should led to the release of two molecules of CO_2. If the formation of sodium bicarbonate is considered, the utilization of the adsorbent results in, i.e., 0.12, 0.37 and 0.36 for 5 wt.%, 10 wt.% and 15 wt.%, respectively.

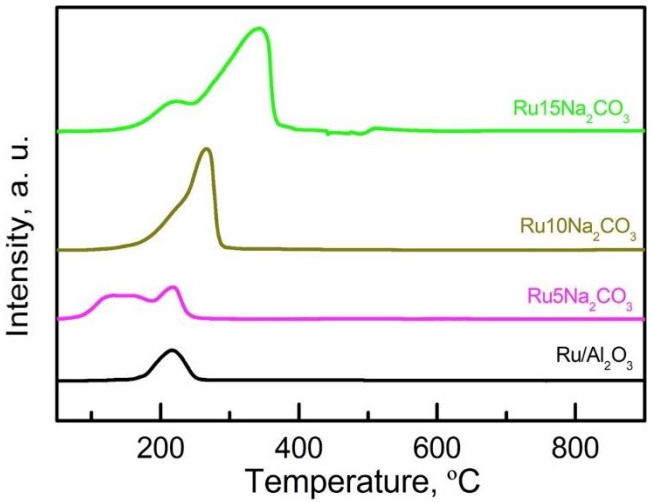

Fig. 12. H2-TPR patterns for Ru-Na2CO3/Al2O3 sample with different adsorbent contents, i.e. 5, 10 and 15 wt.%. Ru/Al2O3 sample is also included as reference.

Fig. 12 shows the H_2-TPR experiments for the prepared samples. A single reduction peak was observed for the reference 4%Ru/Al_2O_3 sample at 200 °C, assigned to the reduction of Ru_xO_y species to Ru^0. Considering that the unique reducible species in the catalyst is Ru and that the noble metal content is the same for all prepared samples, there should be an additional effect to explain the increase of the hydrogen consumption as the adsorbent loading increases.

In order to gain insight into the reduction process, the effluent gas of the H_2-TPR experiment was analyzed by FTIR to quantitatively determine the products of the reduction process. As can be observed in Figure S3, nitrogen and carbon containing products were detected during the H_2-TPR. Nitrogen monoxide (NO) was the first product detected for temperatures higher than 160 °C. The formation of NO is related to the decomposition of residual nitrates belonging to the adsorbent and noble metal precursors that have not been completely decomposed during the calcination step.

Methane formation was also detected during the H_2-TPR. The formation of CH_4 is ascribed to the hydrogenation of the CO_2 adsorbed in the samples, due to the exposure to the environment prior to the experiment. The formation of CH_4 by CO_2 hydrogenation also requires metallic ruthenium. Therefore, the onset temperature for CH_4 detection matches that of NH_3.

CH_4 formation was delayed to higher temperatures with increasing the adsorbent loading, which confirms that the reduction of ruthenium is progressively hindered by increasing loadings of adsorbent.

The H_2 consumption detected during the H_2-TPR cannot be only related to the reduction of the noble metal ($Ru_xO_y+yH_2 \rightarrow xRu + yH_2O$). Thus, the overall increase in the H_2 consumption during the H_2-TPR for increasing adsorbent loadings can be related to a higher production of methane due to pre adsorbed CO_2 in the samples. Besides, the displacement of the H_2 consumption to higher temperatures is linked to a progressive delay in the temperature at which Ru is reduced.

Considering that nitrogen or carbon containing products were not detected during the H_2-TPR for the adsorbent free 4%Ru/Al_2O_3 sample (Figure S3), the H_2 consumption can be exclusively related to the reduction of the noble metal. After integrating and quantifying the hydrogen consumption, the H_2/Ru ratio resulted in 2.0. This result is in agreement with a Ru oxidation state of +4, i.e. RuO_2 ($RuO_2+2H_2 \rightarrow Ru+2H_2O$). The oxidation state of Ru for the samples containing the adsorbent was determined by XPS (Figure S4). For all samples, the XPS spectra were consistent with the presence of Ru^{+4}.

Temperature programmed surface reaction (TPSR) of pre-adsorbed CO_2 with H_2

Fig. 13 shows the production of CH_4 during temperature programmed surface reaction (TPSR) of pre-adsorbed CO_2 with H_2. These experiments were performed by first reducing the catalyst up to 400 °C with 5%H_2/Ar to clean the catalyst surface and reduce the noble metal to Ru^0. Then, the catalyst was saturated with CO_2 at 50 °C, and finally 5% H_2/Ar gas stream was contacted while increasing the catalyst

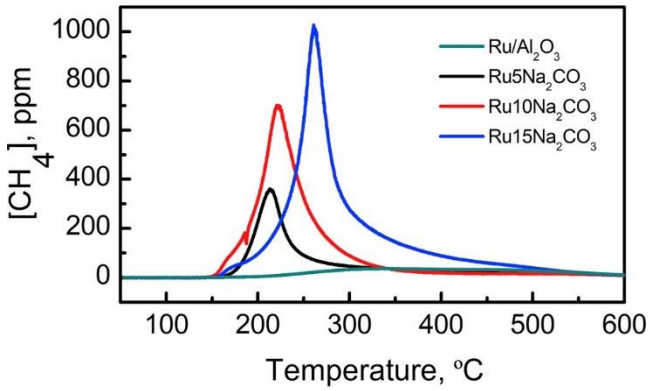

Fig. 13. CH4 formation during temperature programmed surface reaction with pre-adsorbed CO2 onto Ru Na2CO3/Al2O3 samples

Table 14: CH_4 formation during TPSR experiments with pre-adsorbed CO_2.

1) Sample	1) CH_4, kg-mol kg^{-1}	1) CH_4/Na_2CO_3
2) $Ru5Na_2CO_3$	2) 243	2) 0.29
3) $Ru10Na_2CO_3$	3) 462	3) 0.38
4) $Ru15Na_2CO_3$	4) 686	4) 0.41

temperature to 600 °C. In the absence of an adsorbent, i.e. Ru/Al_2O_3 sample, the formation of CH_4 is minor, due to the low ability of the sample to pre-adsorb CO_2, as observed in the CO_2TPD experiment. Table 14 summarizes CH_4 formation during TPSR experiments with all prepared samples.

The catalysts containing Na_2CO_3 as adsorbent presented a unique temperature region for carbonates decomposition and CH_4 production. CH_4 production clearly increases with the Na_2CO_3 loading, i.e., 243 kg-mol, 462 kg-mol and 686 kg-mol for 5, 10 and 15%, respectively. Maximum CH_4/Na_2CO_3 ratio is obtained for the sample with the highest adsorbent loading, i.e. $Ru15Na_2CO_3$, in line with the higher Ru dispersion (19.3%, Table 12).

CO_2 adsorption and hydrogenation mechanism onto Ru-Na_2CO_3/Al_2O_3 catalyst

Fig. 14 shows the concentration profiles of CO_2, H_2O, CH_4 and

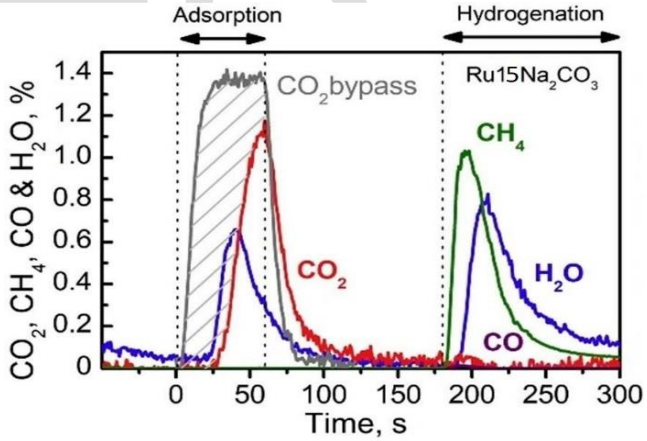

Fig. 14: CO_2, H_2O, CH_4 and CO concentration profiles during one CO_2 adsorption and hydrogenation cycle with

CO at the reactor outlet for one CO_2 adsorption and hydrogenation cycle, once the steady state was reached. The adsorption and hydrogenation cycle are performed by admitting to the reactor a gas stream composed of 1.4% CO_2/Ar during 1 min. Afterwards, the reactor is purged with Ar for 2 min. Finally, the hydrogenation step is carried out with a gas stream composed of 10%H_2/ Ar for 2 min. Fig. 14

also includes the CO_2 concentration profile when the reactor is bypassed. The temporal evolution of reactants and products is qualitatively similar during the CO_2 adsorption and hydrogenation cycles with $Ru15Na_2CO_3$ sample (Fig. 14). However, the adsorption chemistry is not so well understood for sodium carbonate. As already observed for calcium oxide containing catalysts, at the beginning of the storage period, the concentration of CO_2 is negligible. In this period of time the adsorption of CO_2 is complete, and H_2O is not observed in the effluent gas. The following reactions can be used to describe the adsorption of CO_2 without the release of H_2O for sodium containing catalysts:

$$Na_2O + CO_2 \leftrightarrows Na_2CO_3 \quad (27)$$

$$NaOH + CO_2 \leftrightarrows NaHCO_3 \quad (28)$$

Eq. (27) describes the adsorption of CO_2 onto sodium oxide to form sodium carbonate, whereas Eq. (28) yields sodium bicarbonate through carbonation of hydrated sodium oxide. After 30 s of storage time, the adsorption of CO_2 then proceeds with the release of H_2O. The following reaction can be used to describe the adsorption of CO_2 while H_2O is desorbed:

$$2NaOH + CO_2 \leftrightarrows Na_2CO_3 + H_2O \quad (29)$$

As H_2O release is only observed for storage periods longer than 30 s, the extension of Eq. (29) is negligible for shorter storage times. Consequently, as Eq. (28) shares the same reactants than Eq. (29), it can be concluded that the extension of Eq. (28) would be also negligible for short storage periods. Therefore, Eq. (27) results in the unique plausible reaction to describe the CO_2 storage without the release of H_2O during the beginning of the storage step. For longer storage times, once Eq. (29) is running and H_2O and CO_2 are present in the gas stream, the storage of CO_2 could further proceed through the following reaction:

$$Na_2CO_3 + H_2O + CO_2 \leftrightarrows 2NaHCO_3 \quad (30)$$

where the joint adsorption of CO_2 and H_2O onto sodium carbonate yields sodium bicarbonate. The combination of Eqs. (29) and (30) results in Eq. (28), which describes the CO_2 adsorption without the release of H_2O, i.e., H_2O formed through Eq. (29) would be reabsorbed to form sodium bicarbonate through Eq. (30). As H_2O formation has been experimentally observed at the reactor outlet, Eq. (30) is discarded to describe the adsorption of CO_2 onto sodium containing catalysts.

To sum up, the storage of CO_2 is carried out over Na_2O and NaOH species. The presence of Na_2O species in alumina supported samples. First, more reactive
Na_2O species adsorbed CO_2 through Eq. (27) to form Na_2CO_3. Then, when Na_2O species are completely carbonated, the storage of CO_2 can proceed onto NaOH species through Eq. (29), which results in the formation of Na_2CO_3 and the release of H_2O. The formation of sodium bicarbonates ($NaHCO_3$) on the catalyst surface through Eqs. (28) and (30) cannot be ruled out, although the extension of those reactions is limited with respect to Eqs. (27) and (29), which are the main reactions to describe the CO_2 adsorption process based on the temporal evolution of reactants and products shown in Fig. 14. In fact, the presence of sodium bicarbonates has only been confirmed by FTIR at room temperature onto samples with low Na_2CO_3 content (< 3 wt.%). It seems that those bicarbonates are easily decomposed to Na_2CO_3 at higher temperatures through the reverse Eq. (30).

The amount of CO_2 adsorbed onto the catalyst is calculated by Eq. (2). During the storage period, 1235 kg-mol of CO_2 are stored in $Ru15Na_2CO_3$ catalysts. After the storage period, the CO_2 is removed from the feed stream and the catalyst is purged with Ar for two minutes, observing that the CO_2 concentration progressively decreases to practically zero. During this period of time, some of the CO_2 physically adsorbed is released. Consequently, the amount of CO_2 adsorbed before the hydrogenation step is slightly reduced to 926 kg-mol of CO_2.

A very small amount of CO (16 kg-mol) is produced through the RWGS reaction ($CO_2+H_2 \leftrightarrows CO+H_2O$) during the CO_2 hydrogenation step. The amount of CO_2 stored during the adsorption step and the amount of CH_4, H_2O and CO produced during the hydrogenation step are collected in Table 15.

Table 15: Stored CO_2 and released H_2O during the adsorption step and CH_4, H_2O and CO production during the hydrogenation step.

Sample	Storage period			Hydrogenation period		
	Stored CO_2[a], kg-mol kg^{-1}	Released CO_2[b], kg-mol kg^{-1}	Stored CO_2[c], kg-mol kg^{-1}	CH_4, kg-mol kg^{-1}	H_2O, kg-mol kg^{-1}	CO, kg-mol kg^{-1}
$Ru15Na_2CO_3$	1235	309	926	926	1852	17

[a] Stored CO_2 during the CO_2 adsorption step.
[b] Released CO_2 during the purge step with Ar between storage and hydrogenation periods.
[c] Stored CO_2 before the hydrogenation step.

A reaction scheme can be deduced for Na_2CO_3 decomposition and hydrogenation as follows, which is also consistent with the experimental data:

Step 1: $Na_2CO_3 \leftrightarrows Na_2O + CO_2$ (31)

Step 2: $CO_2 + 4H_2 \leftrightarrows CH_4 + 2H_2O$ (1)

Step 3: $Na_2O + H_2O \leftrightarrows 2NaOH$ (32)

Global: $Na_2CO_3 + 4H_2 \leftrightarrows 2NaOH + CH_4 + H_2O$ (33)

The CO_2 decomposition and CH_4 formation is slower for Na_2CO_3 containing catalysts. The
slower CH_4 formation kinetics would have practical implications for the industrial application and would imply the adjustment of the hydrogenation period time for an efficient use of the reductant.

In this case, 398 kg-mol of CH_4 and 454 kg-mol of H_2O are produced during the hydrogenation step and the H_2O/CH_4 ratio results in 1.14, which is also close to the stoichiometry of Eq. (17), and again validates the proposed mechanism to describe the CO_2 adsorption and hydrogenation with Na_2CO_3 containing catalyst. Preliminary experiments by FTIR further corroborate the proposed mechanism for the CO_2 storage and hydrogenation (Figure S5).

Finally, if the CO_2 adsorption and hydrogenation periods are jointly considered, the combination of Eqs. (10) and (17) results in the CO_2 hydrogenation reaction, i.e. Eq. (1). Integrating the H_2O formation in the periods the result obtained is 1852 kg-mol of H_2O for Na_2CO_3 containing catalysts. Thus, the H_2O/CH_4 ratio results in 1.96, close to the value of 2 predicted by the stoichiometry of the CO_2 hydrogenation reaction (Eq. 1). The carbon balance was also adequately closed. The amount of CO_2 stored during the adsorption period are 926 kg-mol of CO_2 stored and 926 kg-mol of CH_4 and 16 kg-mol of CO produced for Na_2CO_3 containing catalyst, which closes the carbon balance in 110%.

Adsorbent loading and temperature effects on CO_2 adsorption and hydrogenation cycles

Increasing the adsorbent loading to 10% and 15% results in a clear promotion of the CO_2 storage and CH_4 production.
Temperature effect is not so noteworthy in the production of CH_4 for catalysts containing 10% and 15% Na_2CO_3. It has been observed by CO_2-TPD experiments that strong basic site are not so abundant, and the strength of those sites is small. Furthermore, TPSR experiments revealed that the regeneration of the storage sites could be obtained at much lower temperature, with CH_4 production peak situated around 300 °C.

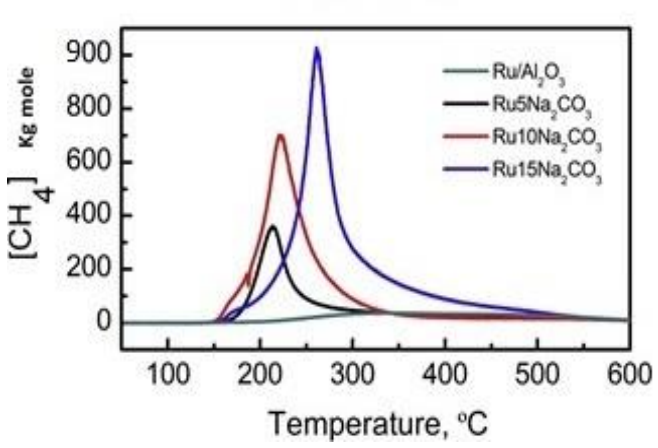

Fig. 15: shows the production of CH_4 during temperature programmed surface reaction (TPSR) of pre-adsorbed CO_2 with H_2. About (926.25 Kg mole)

Maximum CH_4 production is observed at intermediate temperature (320 °C), which could be attributed to a slightly deeper regeneration of the storage sites. The higher dispersion of the Ru for Na_2CO_3 containing samples also has a positive effect in CH_4 production, especially at low temperatures.

Finally, the stability of $Ru15Na_2CO_3$ sample was studied performing 15 consecutive adsorption and hydrogenation cycles at 400 °C (Figure S7). The evolution of CO_2, CH_4 and H_2O was repetitive during the 15 consecutive cycles. CH_4 yield per cycle remained constant, highlighting the stability of the catalyst towards the CO_2 adsorption and methanation reaction.

Conclusions

In this work, we considered computational catalysis leveraged by quantum computing. We rely on accurate error bounds on the electronic energy accessible in quantum algorithms to obtain sufficiently accurate data for intermediate and transition state structures of a catalytic cycle. In particular, i) we considered decisive steps of a synthetic catalyst that is known to convert carbon dioxide to methanol (and for which traditional work based on density functional theory had already been reported alongside the experimental results [1]), ii) we presented a new quantum algorithm in the qubitization framework that exploits a double-factorized electronic structure representation, which significantly reduces the runtime, iii) we validated the truncation schemes by comparison with density matrix renormalization group calculations, iv) we confirmed that starting the quantum algorithm from a single determinant initial state has high success probability for the carbon dioxide functionalization process studied in this work, and v) we calculated realistic resource estimates for mid-term scalable quantum computers and related them to expected runtimes.

A complete reaction scheme describing the CO_2 adsorption and hydrogenation process has been proposed. Total CO_2 adsorption has been observed in the beginning of the storage

period. Afterwards, the CO_2 adsorption proceeds with the release of H_2O. For Na_2CO_3 containing catalysts, the CO_2 is preferentially adsorbed onto Na_2O species and then onto NaOH with the release of H_2O. During the hydrogenation step, CH_4, H_2O and CO are detected. The detection of H_2O is delayed with respect to the beginning of the hydrogenation period, suggesting that H_2O formed through the CO_2 hydrogenation is adsorbed onto the storage sites. CO formation is minor irrespective of the nature of the adsorbent, which highlights the high selectivity of the prepared catalysts towards CH_4 formation.

We've now shown evidence that quantum computers are well-suited to computational chemistry calculations. From Schrodinger's equation to encoding methods, and from encoding methods to VQE, we provided the theoretical foundation that enables the application of quantum computational chemistry and enables SYCAMORE algorithm for addressing climate change

SYCAMORE Supplementary Material:
https://drive.google.com/file/d/1-g0j7vj2T82D4vW8wys064uk87F_gqAi/view?usp=sharing

You can check our website for more information about our project: https://s-y-c-a-m-o-r-e.com

For further information about the paper, we encourage you to see: https://www.ijser.org

ACKNOWLEDGMENTS

We are grateful to Prof. Anthony Hoffman for sharing his insights into the algorithm with us, valuable discussions on the catalyst synthesized in the lab and for providing us with the correct structure of complexes, and to Dr. Yousef Shaban gratefully acknowledge financial support by the Egyptian space Agency (ESA).

[1] Sebastian Wesselbaum, Verena Moha, Markus Meuresch, Sandra Brosinski, Katharina M. Thenert, Jens Kothe, Thorsten vom Stein, Ulli Englert, Markus H¨olscher, J¨urgen Klankermayer, and Walter Leitner, "Hydrogenation of carbon dioxide to methanol using a homogeneous ruthenium–Triphos catalyst: From mechanistic investigations to multiphase catalysis", Chem. Sci. 6, 693–704 (2015)

[2] Krysta M. Svore and Matthias Troyer, "The quantum future of computation", IEEE Computer 49, 21–30 (2016).

[3] Yudong Cao, Jonathan Romero, Jonathan P. Olson, Matthias Degroote, Peter D. Johnson, M´aria Kieferov´a, Ian D. Kivlichan, Tim Menke, Borja Peropadre, Nicolas P. D. Sawaya, Sukin Sim, Libor Veis, and Al´an Aspuru-Guzik, "Quantum Chemistry in the Age of Quantum Computing", Chem. Rev. 119, 10856–10915 (2019).

[4] Sam McArdle, Suguru Endo, Al´an Aspuru-Guzik, Simon C. Benjamin, and Xiao Yuan, "Quantum computational chemistry", Rev. Mod. Phys. 92, 015003 (2020).

[5] Daniel S. Abrams and Seth Lloyd, "Simulation of Many-Body Fermi Systems on a Universal Quantum Computer", Phys. Rev. Lett. 79, 2586–2589 (1997).

[6] Kandala, A., Mezzacapo, A., Temme, K. et al. Hardware-efficient variational quantum eigensolver for small molecules and quantum magnets. Nature 549, 242–246 (2017).

[7] J.V. Veselovskaya, P.D. Parunin, A.G. Okunev, Catalytic process for methane production from atmospheric carbon dioxide utilizing renewable energy, Catal. Today 298 (2017) 117–123.

[8] M. Shokrollahi Yancheshmeh, H.R. Radfarnia, M.C. Iliuta, High temperature CO2 sorbents and their application for hydrogen production by sorption enhanced steam reforming process, Chem. Eng. J. 283 (2016) 420–444.

[9] C. Janke, M.S. Duyar, M. Hoskins, R. Farrauto, Catalytic and adsorption studies for the hydrogenation of CO2 to methane: Environ. 152-153 (2014) 184–191.

[10] Q. Zheng, R. Farrauto, A. Chau Nguyen, Adsorption and Methanation of Flue Gas CO2 with Dual Functional Catalytic Materials: A Parametric Study, Ind. Eng. Chem. Res. 55 (2016) 6768–6776.

[11] M.S. Duyar, S. Wang, M.A. Arellano-Treviño, R.J. Farrauto, CO2utilization with a novel dual function material (DFM) for capture and catalytic conversion to synthetic natural gas: an update, J. CO2 Util. 15 (2016) 65–71.

[12] L.F. Bobadilla, J.M. Riesco-García, G. Penelás-Pérez, A. Urakawa, Enabling continuous capture and catalytic conversion of flue gas CO2to syngas in one process, J. CO2 Util. 14 (2016) 106–111.

[13] Dave Wecker, Matthew B. Hastings, and Matthias Troyer, "Progress towards practical quantum variational algorithms", Phys. Rev. A 92, 042303 (2015).

[14] Nathan Wiebe and Chris Granade, "Efficient bayesian phase estimation", Phys. Rev. Lett. 117, 010503 (2016).

[15] Michael A. Nielsen and Isaac L. Chuang, Quantum Computation and Quantum Information, 1st ed. (Cambridge University Press, 2004).